DESIGN AND MODELLING OF HALF BRIDGE LLC RESONANT CONVERTER AND SEPIC CONVERTER FOR ON BOARD FORWARD AND BIDIRECTIONAL CHARGING OF EV BATTERY

A DISSERTATION

SUBMITTED IN PARTIAL FULFILLMENT OF THE RQUIREMENTS
FOR THE AWARD OF THE DEGREE
OF

MASTER OF TECHNOLOGY
IN
POWER ELECTRONICS AND SYSTEM

Submitted by:

RAHUL MAURYA
2K20/PES/16

Under the supervision of

PROF. RADHESHYAM SAHA

DEPARTMENT OF ELECTRICAL ENGINEERING
DELHI TECHNOLOGICAL UNIVERSITY
(Formerly Delhi College of Engineering)
Bawana Road, Delhi-110042

JUNE,2022

DEPARTMENT OF ELECTRICAL ENGINEERING
DELHI TECHNOLOGICAL UNIVERSITY
(Formerly Delhi College of Engineering)
Bawana Road, Delhi-110042

CANDIDATE'S DECLARATION

I, Rahul Maurya, Roll No. 2K20/PES/16 student of MTech (Power Electronics and Systems), hereby declare that the project Dissertation titled "**Design and modelling of half bridge LLC resonant converter and SEPIC converter for on board forward and bidirectional charging of EV battery**" which is submitted by me to the Department of Electrical Engineering, Delhi Technological university, Delhi in partial fulfilment of the requirement for the award of the degree of Master of Technology, is original and not copied from any source without proper citation. This work has not previously formed the basis for the award of any Degree, Diploma Associateship, Fellowship or other similar title or recognition.

Place: Delhi — Rahul Maurya

Date: 31 May 2022 — (2K20/PES/16)

DEPARTMENT OF ELECTRICAL ENGINEERING
DELHI TECHNOLOGICAL UNIVERSITY
(Formerly Delhi College of Engineering)
Bawana Road, Delhi-110042

CERTIFICATE

I hereby certify that the project Dissertation titled "**Design and modelling of half bridge LLC resonant converter and SEPIC converter for on board forward and bidirectional charging of EV battery**" which is submitted by Rahul Maurya, Roll No. 2K20/PES/16, Department of Electrical Engineering, Delhi Technological University, Delhi in partial fulfilment of the requirement for the award of the degree of Master of Technology, is a record of the project work carried out by the student under my supervision. To the best of my knowledge this work has not been submitted in part or full for any Degree or Diploma to this University or elsewhere.

Place: Delhi — Prof. Radheshyam Saha

Date: 31 May 2022 — SUPERVISOR

DEPARTMENT OF ELECTRICAL ENGINEERING
DELHI TECHNOLOGICAL UNIVERSITY
(Formerly Delhi College of Engineering)
Bawana Road, Delhi-110042

ACKNOWLEDGEMENT

I wish to express my sincerest gratitude to **Dr Radheshyam Saha** for his continuous guidance and mentorship that he provided me during the proposed research work. He showed me the path to achieve our targets by explaining all the tasks to be done and explained to me the importance of the research topic as well as its industrial relevance. He was always ready to help me and clear my doubts regarding any hurdles in this project. Without his constant support and motivation, this research work would not have been successful.

Place: Delhi Rahul Maurya

Date: 31 May 2022

Abstract

The combustion of fossil fuels, a non-renewable and limited resources, has caused global warming, ozone damage, air pollution and acid rain. Electric vehicles are eco-friendly with attractive features such as, less emission of greenhouse gases, lower fuel usage and reduced air pollution. The battery charger is one of the most important components of the electric vehicle. This research work focusses on the on-board battery charger.

Firstly, a Half-Bridge LLC resonant converter topology is designed which owns soft-switching features, high efficiency, and regulated output voltage. The output voltage is well regulated with the help of conventional PI-controller. It has been also simulated for the all the three modes, at resonance frequency, below resonance frequency and above resonance frequency in order to identify the optimal operating point of the converter.

Secondly, the half-bridge LLC resonant converter is integrated with the boost converter to improve the power quality. The boost converter has been employed for the power factor correction. The output voltage is controlled with the PI-controller. The steady state and dynamic performance are analysed in MATLAB software under load and input supply variations.

Further improvement has been done to supress the large inrush current observed in boost PFC by replacing boost converter with SEPIC converter. The presence of intermediate capacitor helps to supress the inrush current. There are some other unique features also introduce such as, it always operates near the resonance frequency for different output voltage, it also has the capability to give excellent performance under various input supply voltage, different loads at output.

Nevertheless, a bidirectional half-bridge LLC resonant converter is designed which can perform in both forward mode and backward mode. In forward mode, the battery charging has been done and in backward mode, battery supply the power load connected at the supply side of the converter. The bidirectional LLC resonant converter has capability of soft-switching in both the forward and backward mode of operations. In forward mode, control of battery charging has been done with the help of PI-controller and in backward mode the voltage across the load is regulated with the PI-controller.

Contents

List of Tables

List of Figures

List of Symbols

C_r	Resonant capacitor
L_r	Resonant inductor
L_m	Magnetizing inductor
F_x	Normalized switching frequency
f_r	Resonant frequency (series)
f_p	Resonant frequency (Parallel)
Q	Quality factor
R_{ac}	Reflected load resistance
m	Inductance ratio
fs	Switching frequency
Np, Ns	Primary and Secondary turns
Ro	Load Resistance
P_{in}	Input power
P_0	Output power
V_{in}^{max}	Maximum input voltage
V_{OPFC}	Output voltage of PFC
V_{in}^{min}	Minimum input voltage
M^{min}	Minimum gain of LLC
M^{max}	Maximum gain of LLC
n	Turns ratio
f_{min}	Minimum frequency
K_p	Proportional gain
K_i	Integral gain
ΔV_d	Ripple of DC-link voltage
ΔI_{L1}	Current ripple of inductor
V_d	DC link voltage
D	Duty ratio
L_1	Primary inductor of boost converter
C_d	dc- link capacitor
V_{dc}	DC-link voltage of SEPIC
Ω	Normalized frequency
M_f	Forward gain of LLC
M_b	Backward gain of LLC

CHAPTER 1
LITERATURE SURVEY

1.1 Introduction of Electric Vehicles

The global energy utilization due to transportation is predicted to increase by around 45 percent from 2009 to 2036 [1]. This utilization is accountable for the major share (63%) of the total rise in petroleum and other fossil fuels usage from 2010 to 2040. The combustion of a non-renewable, fossil fuels and finite resource, has caused, acid rain, ozone damage, increasing air pollution and global warming. Consequently, new technologies for substitute vehicles are of great curiosity to researchers, governments, industry, and the general public these days [2,3].

Electric vehicles (EVs) are propelled by electric motors and are powered directly from an energy store rather than indirectly via internal combustion engines (ICEs) [2, 3]. EVs are more eco-friendly than typical fossil fuel-powered vehicles, with lower fuel consumption, lesser carbon emissions, and lesser air pollution [4]. As a result, EVs are gaining popularity around the world.

Apart from the ability to resolve environmental deprivation and the fossil fuel problem, another benefit of electric vehicles is that they can be utilized as energy storage units in vehicle-to-grid (V2G) applications as well as traditional grid-to-vehicle (G2V) charging [5, 6]. V2G technology's fundamental idea is to employ vehicles as energy storage units and give electricity to the grid to assist the grid during voltage and frequency dips [7, 8]. When a considerable amount of grid electricity is generated from renewable energy sources with a high degree of variation, such as wind, solar, and wave/tide, this support may become critical.

Overall, based on this extensive literature survey [1-69] the research work has been simplified for forward and bidirectional charging of batteries for electric vehicles.

1.2 Batteries for Electric Vehicles

Although electric vehicles have advantages, technology limitations such as larger costs than equivalently sized petrol engines, long charging times, restricted battery life, and limited travel distance on a single charge [9].

The safety, power density (power, volume, and weight), reliability, affordability, and life lifetime of an electric vehicle battery are the most important

factors to consider. Firstly, safety is always the priority for the EV [10]. Over-current, over voltage, over temperature, deep discharge, and cell charge balancing are all important protection conditions. Second, because EVs have limited space, power density is a bigger issue. The amount of energy stored in an EV battery is measured in amp-hours (Ah), which defines the vehicle's range. The rate of charging and discharging is determined by current and expressed in Ampere-hour. Finally, the battery life span can be assessed in two ways: minimum calendar life and total charging/discharging cycle life [11]. A vehicle battery is typically expected to last 10-15 years with a specific capacity [12]. Overall, while trade-offs must be considered, an EV battery should meet all of these needs at a reasonable cost, as the high cost of batteries has previously been a significant obstacle to the broad acceptance of electric vehicles [13].

Currently, three main battery technologies are extensively utilised in EVs: lead-acid batteries, nickel metal hydride (NiMH) batteries, and lithium-ion (Li-ion) batteries, the key properties of which are listed in Table 1.1 [14].

Table 1.1 The comparison of Batteries for electric vehicles [14]

Type	**Cost**	**Energy density**	**Discharge power capacity**	**Self-discharge rate**	**Life span**
Lead-acid	Reasonable	Low	Good	High	Short
NiMH	High	High	Good	High	Long
Li-ion	Reasonable	High	Good	Low	Long

The lead-acid battery that powered early electric vehicles like the GM EV1 [15, 16]. It has a high discharge power capacity that allows it to respond quickly to load fluctuations. Meanwhile, due to the progressive technological development, the price is reasonable. However, it is not ideal for the current EVs due to its heavy-weight, low energy density, and limited life period due to deep discharging degeneration.

Toyota Prius [17] and Honda Insight [18] both use NiMH batteries. A NiMH battery offers a higher power density than a lead-acid battery because the charge/discharge operations are simpler. The EV with a NiMH battery has double the driving range as the comparable lead-acid battery due to the high-density feature [19]. A NiMH battery also has a longer life cycle since it can withstand moderate overcharges and severe discharges. Because the NiMH battery has a low internal

resistance and a significantly higher charge acceptance capability, the charging efficiency is higher. The biggest disadvantage of NiMH is its rapid self-discharge rate, which means that while the battery is not in use, it will lose charge. It also has a higher cost and a lower charge acceptance capability in high temperatures, lowering charging efficiency.

For newer generations of EVs, such as the Nissan Leaf [20, 21], lithium-ion (Li-ion) batteries have become one of the preferred energy storage units. Although the Li-ion battery has problems that need to be addressed, cell balance, such as cell life, cooling operation, safety, and cost. It has the advantages of higher energy density, higher power rating (high cell voltage and output power), lower weight, and greater discharging power for faster acceleration when compared to other rechargeable batteries. The following are some of the advantages [12, 22-25]:

1. One of the most appealing features is the higher power density. Li-ion batteries are substantially lighter than other types of batteries when it comes to providing the same level of capacity. For example, the AC Delco lead-acid battery pack in the Chevrolet Volt weighs 590 kg to provide the same amount of energy (16kWh), whereas the new Li-ion battery pack weighs only 170 kg, or 28.81 percent less than the original option.
2. Lithium-ion cells have a self-discharge rate of 2 to 3 percent per month, which is substantially lesser than Lead Acid (4 to 6 percent per month) and NiMH (30 percent per month). As a result, the Lithium-ion battery has a longer life expectancy than other types of batteries. Furthermore, the Lithium-ion battery's discharge curve is impartially flat. It is commonly understood that if the battery's power output drops quickly during the discharge cycle, a dangerous problem can arise towards the end of the cycle, particularly for high-power applications. The Lithium-ion battery, as illustrated in Fig. 1.1, offers essentially constant voltage (corresponding stable power) for about 80% of the discharge cycle.
3. The inside of a Li-ion battery pack has a high number of cells [26]. The 196 cells in the Nissan Leaf battery pack, for example, are made up of 48 modules, each with four cells [27, 28]. The charging process is faster and more efficient with this arrangement.

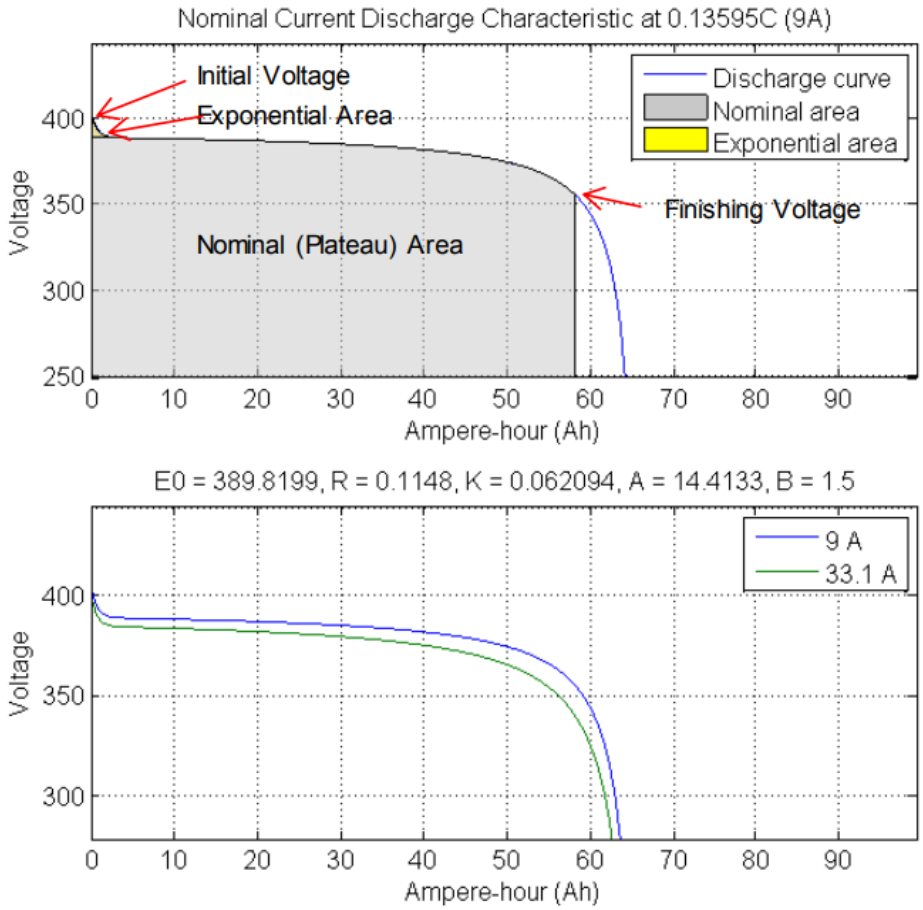

Fig.1.1 The Li-ion battery discharge characteristics [24,30]

1.3 Battery charging Technology

The discharging and charging regulation, as well as the battery design, have an impact on battery performance. Consequently, battery discharge and charge operation and control are important technologies in the whole electric vehicle system [29].

1.3.1 Charging strategy

Constant current (CC) [30], constant voltage (CV) [31], constant power, taper current, and other charging methods exist [32]. The constant voltage charger is the most basic technique for charging a battery. It works by giving the suitable current to sustain a constant battery voltage. To protect the battery, it requires an additional circuit. A constant current charger feeds a fixed current into the battery (typically the maximum current for fast charging), and the battery voltage increases linearly over time. In a slow charging technique, a constant power charger is usually used for large and expensive batteries. When charging in a household context, the key restriction is the maximum current, which must be less than the single-phase outlet fuse current.

The constant current-constant voltage (CC-CV) charging strategy is commonly used for Li-ion batteries [33, 34]. The charging method in this CC-CV charging profile has two stages: CC mode and CV mode. The first stage is the CC mode, in which the current is regulated at a constant value (typically the highest current that the battery can sustain without causing harm) while the battery voltage rapidly increases to its rated maximum level. Continued constant current charging will result in overcharging and excessive heating, potentially damaging the battery. To avoid this, the charging process is switched to CV mode when the battery voltage hits the threshold voltage (almost fully charged voltage), during which the battery voltage is kept at a constant value while the battery is gently charged. Meanwhile, the battery charging current drops to prevent overcharging until it hits a predefined low value, at which point the charging operation is stopped. The maximum charging voltage of a Li-ion battery cell, for example, is commonly 3.6V or 4.2V. The CV stage begins when the battery voltage hits 90% state of charge (SOC) and the current starts to drop [35].

1.3.2 Charging power levels

Battery chargers are categorized into three types [36, 37] based on different power ratings and charging times: Level 1 for slow (domestic) charging, Level 2 for primary charging, and Level 3 for fast charging (typically using DC voltage) [9], as shown in Table 1.2.

Table 1.2 Comparison of charging power levels [36, 38]

Type	Classification	Voltage	Power level	Charging time
Level 1	Slow charging	120V @ AC	2 kW	10-12 Hours
Level 2	Primary charging	240V @ AC	19.2 kW	4 Hours
Level 3	DC fast charging	200V-800V @ DC	50kW- 120kW	Less than 1 hour

Level 1 charging is the most basic EV charging level. It is powered by a typical 120 V household socket and has a range of 4 to 5 miles after an hour of charging. Because most EV manufacturers include a Level 1 EVSE wire set, no additional charging hardware is necessary. Recharging a completely depleted EV battery takes about 20 hours [39]. The use of a 220 V inventory framework is mostly limited to North, South, and Central America, Europe, and a big section of the world. This type

of charging mechanism requires an installation cost of around 39k-62k thousand rupees [500-800 USD].

Level 2 charging equipment uses a private 220 V supply system or a 208 V charging station outside [39]. In an hour of charging, a 3.3 KW on-board charger can provide roughly 15 miles of travel. A 6.6 KW on-board charger, on the other hand, may travel 30 miles in the same amount of time as it takes to charge. Level 2 EVSEs employ equipment specifically designed to speed up recharging and require skilled electrical installation using a dedicated electrical line. The Level 2 charging system will cost around 77k-232k in Indian rupees [1000-3000 USD].

A 480 V AC supply system is required for Level 3 charging. This type of charger may travel 80-100 miles in 20-30 minutes after charging. The DCFC converts AC power to DC, which is then transmitted straight to the EV battery pack. This level of billing is only appropriate for commercial use, not domestic. The cost of execution ranges from 23lakh – 1,24Cr [30000 – 160000 USD].

1.3.3 Off- board and On-board charger

Battery chargers for electric vehicles are often divided into on-board and off-board categories, as indicated in Table 1.3. Off-board chargers, also known as standalone fast-charging stations, function similarly to filling stations for liquid fuel vehicles, providing high-power charging at a rapid rate [9]. Off-board recharge stations, which can considerably expand the range of pure-battery EVs, are typically built-in public areas such as shopping malls, car parks, and highway facilities [40]. The size, weight, and space constraints for developing such an off-board station are lessened; however, these stations require large investment and long-term development time.

On-board chargers, on the other hand, are built into the vehicles and provide modest charging times of 6-16 hours at low power levels of 2-20 kW [9]. When electric vehicles are hooked into a household utility socket overnight, on-board chargers allow straightforward charging. Because the charger can be built within the EV, it will not be as expensive as an off-board charger station. Despite the fact that size, weight, and space limits limit the input power level, making charging slow, on-board charging remains a potential alternative due to its small form, ease of use, and low cost.

Table 1.3 Comparison of off-board and on-board charger

Classification	Power rating	Level type	Charging time	Size limit
Off-board	50kW	3	Less than 1 hr	less
On-board	2-20kW	1,2	4-12 hrs	Yes

According to the SAE J1772 standard [26], on-board chargers often use Level 1 and Level 2, which are intended to be mounted in the vehicle, while off-board chargers typically use Level 3.

1.4. Design requirement of EV battery charger

The research work primarily focuses on the onboard charger which typically consists of two stages, front end PFC and dc-dc converter. The prime objective while designing an onboard charger is:

- Unity power factor for better power quality
- Zero voltage switching leading to High efficiency
- Reduction in size and weight of the charger
- High power density
- Isolation at the output end for enhanced safety

1.4.1 Power Quality

The full-bridge rectifier present on the input side of the converter makes the input current at the converter end out of phase from the source voltage resulting in poor power quality. The converter operating in a discontinuous mode often reduces the power quality at the input side of the source which needs to be improved as per IEEE standards and regulations enforced by various power supply units. A way to improve the power quality is by using a power factor correction circuit.

1.4.2 High efficiency

Major losses are categorized as switching losses and conduction losses. At high-frequency operation, the switching losses predominate the conduction losses. To reduce the switching losses at the high frequency, the primary switch is turned on/off at zero voltage (ZVS) and/or zero current (ZCS) condition avoiding any switching losses. With the advent of Silicon carbide and Gallium nitride technology, $R_{ds(on)}$ of the primary switches are reduced considerably which ultimately could reduce the conduction losses. Another approach to reducing the conduction losses is to replace the diodes at the rectifier with MOSFET, commonly known as synchronous switching. Through ZVS/ZCS switching losses can be avoided and through synchronous rectification conduction losses can be avoided resulting in high efficiency across the converter operation.

1.4.3 Galvanic Isolation

In an electric vehicle system, safety is paramount. Insulation and galvanic isolation should be preserved throughout the battery charger facility life in every working situation, according to ISO 6469-3:2011-2012 [41] and UL2231-1:2002-05 [42]. To guarantee galvanic isolation and safe operation, an isolated transformer is commonly used between the EV battery and the grid [43]. As a result, despite the benefits of low cost, simple structure, small size, light weight and fewer components, [40], the non-isolated DC-DC converters such as boost converter and buck converter [44] will not be used in this research. Furthermore, isolated converters with varying transformer turns ratios have the ability to give a wider output voltage to cope with a wide range of battery voltage in a battery charging systems [45].

1.4.4 Wide operation range

Full-bridge soft-switching topology, such as the dual active bridge (DAB) topology, have been the subject of extensive research [46-48]. The galvanic isolation, symmetrical structure, and bidirectional power transfer capability of the DAB converter are all advantages. The operational zone in which the circuit preserves ZVS narrows as the load lightens, hence ZVS may be lost under light load, which is a disadvantage of the DAB architecture [49]. Furthermore, the DAB circuit's substantial turn-off current and circulating energy result in considerable power loss and reduced efficiency [50].

With ZVS and ZCS [51-55], resonant converters with low electromagnetic interference (EMI) and high efficiency can be employed to produce minimal switching loss. To achieve the zero-crossing of the voltage or current, different numbers of resonance elements are commonly employed to build the resonant tank. The conventional types of resonant converters are series resonant converter (SRC), which comprises two resonant elements in series, parallel resonant converter (PRC), which comprises two resonant elements in parallel, and Series Parallel Resonant Converter (SPRC), which contains three resonant elements, as depicted in Fig. 1.2.

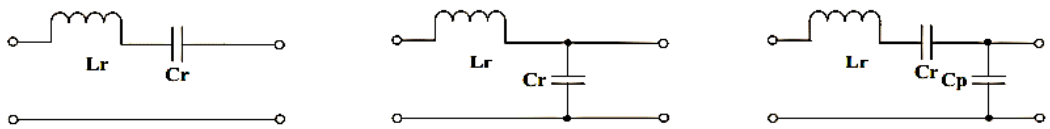

Fig. 1.2 Basic resonant circuit topologies

Overall, given a wide input range and light load situation, the SRC, PRC, and SPRC will have high switching losses, high circulating current, and high conduction loss limiting their capacity to attain high efficiency.

1.4.5 LLC Resonant Converter

The typical resonant circuit of an LLC resonant converter is comprising of a series capacitor, a series inductor and a parallel magnetizing inductor as depicted in Fig.1.3. [56]. Because of the three elements, the whole operation of the LLC resonant converter has two frequencies. One frequency which is related to the series capacitor and series inductor which is known as series resonance frequency and other is related to the all the three elements of the LLC resonant converter series capacitor, series inductor and magnetizing inductor and this frequency is recognized as fundamental resonance frequency. The LLC resonant converter shows the same behavior when it operates above the series frequency. Otherwise, it behaves same as of parallel resonant converter when the load is light and as a series resonant converter under heavy loads. The peak gain of the LLC resonant converter occurs when converter operates between the fundamental resonance frequency and series resonance frequency. When the operation of the LLC resonant converter is above the series resonance frequency, the resonant converter can attain soft-switching features such as zero voltage switching and zero current switching which helps in reducing the conduction losses and switching losses [58,59].

In DC-DC converter with the LLC resonant circuit the zero-voltage switching has been achieved in the primary side active switches and zero current switches in the rectifier diodes for the entire load conditions as well as for no load condition [60,61]. As a result of the advantages discussed, LLC resonant converter is a suitable topology as a DC-DC converter and it is used as for battery charging purpose in this research work.

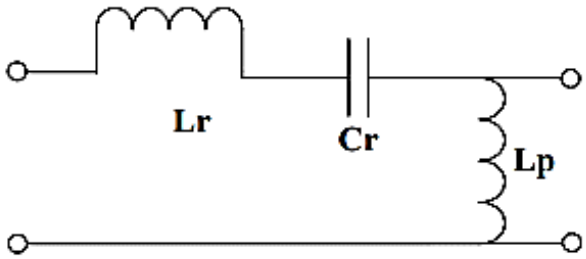

Fig. 1.3 LLC resonant tank

1.5 Motivation

The main goal of this study is to design and modelling an on-board battery charging system for electric vehicles which can work at high efficiency and over a wide range of battery voltages. The LLC resonant converter would be used as the initial design. The major goal is to improve the power quality at supply side of the converter through extensive work in following areas:

1). Analysis of LLC resonant converter

In order to design an optimal on-board battery charger, the LLC resonant converter should be analyzed for different modes of operation to identify the best operating mode.

2) Analysis of dc-dc converter for power factor correction

The problem of large inrush current in boost topology is being analyzed and proposed solution is identified.

1.6 Outline

The thesis is systematized in 7 chapters. The summery of each chapter is given as:

Chapter 1 covers the basics of electric vehicles and battery chargers. Basic EV charger needs are briefly defined, and candidate charger topologies are evaluated. The LLC resonant converter architecture is initially chosen as the battery charger.

Chapter 2 covers the basic of LLC resonant converter and studied for three modes of operations resonance mode, below resonance mode, and above resonance mode.

Chapter 3 presents the boost converter fed LLC resonant converter, where boost converter is utilized for the power factor correction and LLC resonant converter facilitate the battery charging.

Chapter 4 covers the SEPIC converter fed half-bridge LLC resonant converter for battery charging, SEPIC is used for power factor correction which solved the problem

of large inrush current occurs in boost converter and half-bridge LLC resonant converter is used for battery charging purpose.

Chapter 5 discussed the bi-directional LLC resonant converter, backward mode and forward mode of operation is simulated. Forward mode for battery charging application in which power flow from DC-link to battery and in backward mode the power flow from battery to the load connected at DC-link.

Chapter 6 covers sensitive analysis of proposed research work on Half-bridge LLC resonant converter, onboard battery charger based on boost and LLC resonant converter, onboard battery charger based on SEPIC and LLC resonant converter, and bidirectional HB-LLC resonant converter.

Chapter 7 summaries the research work on on-board battery charger for Electric Vehicle, subsequently the future scope of the work.

CHAPTER 2

HALF BRIDGE LLC RESONANT CONVERTER

2.1 Introduction

Half-Bridge DC-DC converters with high-frequency galvanic isolated transformer is commonly employed in the DC-DC stage of a typical on-board electric vehicle battery charging system, as depicted in Fig. 2.1 [9] and Fig.2.2 to provide galvanic isolation between the dc-link and electric vehicle battery.

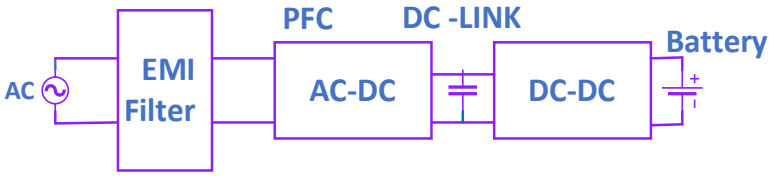

Fig. 2.1 Typical battery charging system

2.2 Objective

The basic operation of Half-Bridge LLC resonant converter for all the three modes of operation:

1. Below resonance mode
2. Resonance mode
3. Above resonance mode

2.3 Overview of LLC Resonant Converter

2.3.1. Architecture of LLC

A Half-Bridge LLC Resonant DC-DC converter is shown in Fig.2.2 with parallel magnetizing inductor L_m , series resonant capacitor C_r, and series resonant inductor L_r . It has three components as follows:

- Square Wave generator
- Resonant Network
- Rectifier Network

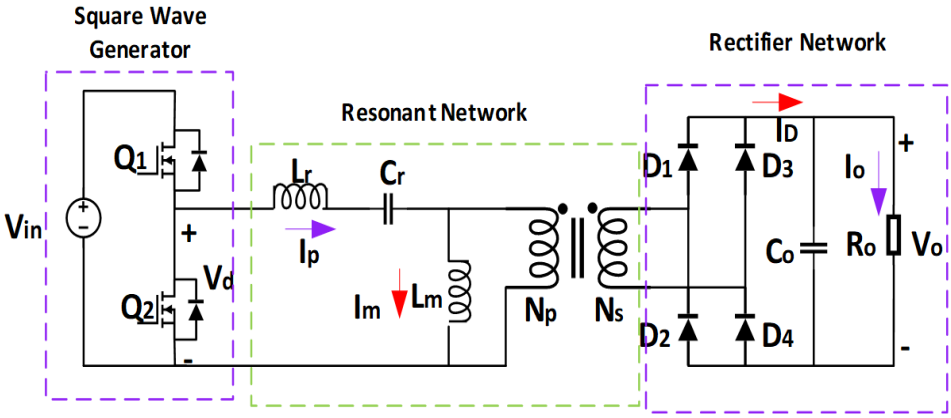

Fig.2.2 Half-Bridge LLC Resonant Converter

Square Wave Generator: Square wave voltage, V_d is generated by the Half-Bridge by driving the MOSFET switches Q_1 and Q_2 interchangeably with a duty cycle of 50 % for both the switches. Between each transition, a very small dead time of order 10ns-15ns is frequently introduced.

Resonant Network: It comprises of resonant capacitor C_r, resonant inductor L_r and magnetizing inductor L_m. The energy is circulated and passed to the load through the transformer by the resonant network. At the transformer primary side, a bipolar square wave is received and this voltage is passed at the secondary winding of the transformer having the turn ratio for the desired output voltage.

Rectifier network: A full-bridge rectifier uses diodes ($D_1 \ldots D_4$) and capacitors with a capacitive output filter to convert the AC voltage to DC voltage.

2.4 Design Specification

The design process for the proposed DC-DC Converter involves the following specifications:

- Maximum Input Voltage (V_{in}^{max}): 420 V DC
- DC-Link Capacitor ($C_{DC\text{-}LINK}$): 470uF
- Rated Output Voltage (V_o): 58V DC
- Maximum Output Power (P_o): 696 Watts
- Hold-up time (T_H): 20ms (50 Hz line frequency)

2.4.1 Gain of LLC Resonant Converter

Fig. 2.3 (a) represents the non-sinusoidal circuit and Fig.2.3 (b) shows the sinusoidal circuit based on First Harmonic Approximation (FHA) as illustrated in [62].

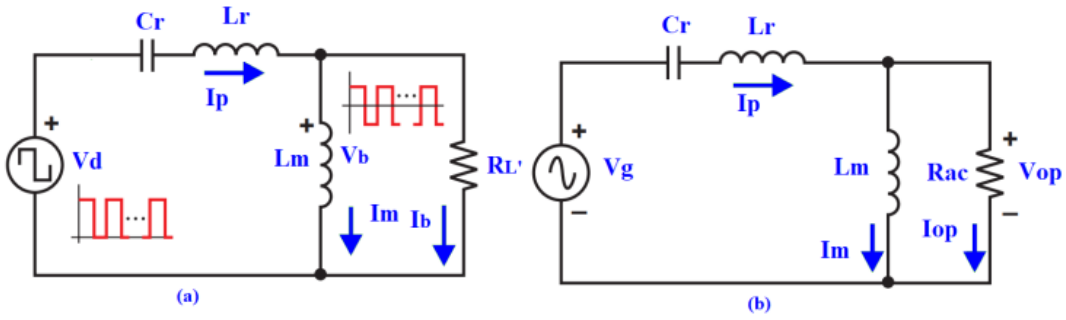

Fig. 2.3 First Harmonic Approximation (FHA)

The transfer function of the converter is the gain of the resonant converter (M) that can be determined from the circuit depicted in Fig. 2.3 (b)

$$M = \frac{V_{op}(s)}{V_g(s)} \tag{2.1}$$

$$M = \frac{sL_m \,||\, R_{ac}}{(sL_m \,||\, R_{ac}) + sL_r + 1/sC_r} \tag{2.2}$$

Where V_{op} is primary voltage, V_g is fundamental voltage of V_d.

The fundamental input voltage (V_g) can be given as:

$$V_g(t) = \frac{2}{\pi} \times Vin \times \sin(2\pi f_s t) \tag{2.3}$$

The RMS value of Vg:

$$V_g = \frac{\sqrt{2}}{\pi} V_{in} \tag{2.4}$$

The fundamental voltage of V_b is given as V_{op}:

$$V_{op} = \frac{4n}{\pi} V_0 \times \sin(2\pi f_s t - \theta v) \tag{2.5}$$

Where n is the turn ratio of the transformer and θv is the phase angle between V_{op} and V_g.

The RMS value of V_{op} can be determined as:

$$V_{op} = \frac{2\sqrt{2}}{\pi} \times n \times V_0 \tag{2.6}$$

The gain in terms of V_{in} and V_o can be determined by dividing (2.6) by (2.4),

$$M = \frac{V_{op}}{V_g} = \frac{2nV_0}{V_{in}} \tag{2.7}$$

The magnitude of gain is:

$$M = \left| \frac{m \times {F_x}^2}{[(m+1) \times F_x^2 - 1] + j(F_x^2 - 1) \times F_x \times Q \times m} \right| \tag{2.8}$$

Regardless of load variation, the gain at the resonant frequency (f_r) remains constant:

$$M = \frac{2nV_o}{V_{in}} \; at \; f_s = f_r \tag{2.9}$$

All parameters and related equations are summarised in Table 2.1.

Table 2.1 Equations for Resonant Converter Parameters

Variable	Formula	Parameters
F_x	$\frac{f_r}{f_s}$	Normalized switching frequency
f_r	$\frac{1}{2\pi\sqrt{L_r C_r}}$	Resonant frequency (Series)
f_p	$\frac{1}{2\pi\sqrt{(L_m + L_r)C_r}}$	Resonant frequency (Parallel)
Q	$\frac{\sqrt{Lr/Cr}}{R_{ac}}$	Quality factor
R_{ac}	$\frac{8}{\pi^2} \cdot \frac{N_P^2}{N_S^2} \cdot R_0$	Reflected load resistance
m	$\frac{L_m}{L_r}$	Inductance ratio
fs		Switching frequency
Lm	$\frac{2\pi f_r m Q N_s^2}{N_p^2 R_o}$	Magnetizing Inductor
Lr	$\frac{1}{(2\pi f_r)^2 C_r}$	Resonant Inductor
Cr	$\frac{1}{2\pi Q f_r R_{ac}}$	Resonant Capacitor
Np, Ns		Primary and Secondary turns
Ro	$\frac{V_0^2}{P_0}$	Load Resistance

2.4.2 Modes of Operation

LLC operation can be categorised into three modes [63] based on switching frequency as indicated below

- **$f_s = f_r$** (Resonance Mode)
- **$f_s > f_r$ (**Buck Mode)
- **$f_s < f_r$** (Boost Mode)

At resonance frequency ($f_s = f_r$), the normalized frequency (F_x) is equal to 1 i.e., $f_r = f_s$. The resonant current (I_p) meets the current flowing through the magnetizing

inductor (I_m) when switch Q_1 is turned off, and no power is passed to the secondary side. The switch Q_2 delays turn-on time to attain the input side Zero Voltage Switching (ZVS) and soft commutation of the rectifier diodes on the output side.

At buck mode ($f_s > f_r$), the current flowing in resonant tank is smaller which reduces the conduction loss. The resonant current (I_p) is in Continuous Current Mode (CCM) which result in less RMS current for the same amount of load. The diodes on the secondary side of the transformer are not softly commutated, and reverse recovery losses occur. However, operation for frequencies greater than the resonance frequency can still achieve ZVS on the primary side. Operation in Buck mode may cause significant frequency increase under light load conditions.

At boost mode ($f_s < f_r$), the resonant current (I_p) meets the magnetizing current (I_m) before the end of the driving pulse width. Even though the magnetizing current (I_m) continues, the power transfer stops. The ZVS on the input side and soft commutation of the rectifier diodes on output side can still be achieved. The current in rectifier diode on the secondary side is in Discontinuous Current Mode (DCM) and require more circulating current in the resonant tank circuit for the same load, resulting in high conduction loss on both the secondary side and primary side. Operation below the switching frequency, if the switching frequency is too low, the ZVS on the primary side may be lost.

2.4.3. Computation of Design Parameters

The design parameters are calculated for resonance mode taking resonant frequency f_r =100 kHz.

Input Power:

Taking efficiency into account, E_{ff} = 96%, maximum input power (P_{in}) is calculated as follows:

$$P_{in} = \frac{P_0}{E_{ff}} = \frac{696}{0.96} = 725\ W \tag{2.10}$$

Input Voltage (V_{in}^{min} and V_{in}^{max}):

The maximum input voltage is the PFC output voltage (V_{OPFC}). Generally, boost converter is used in PFC. Thus,

$$V_{in}^{max} = V_{OPFC} = 420V \tag{2.11}$$

Considering the Hold-up time (T_H) i.e., the time required to maintain regulated voltage at the output of PFC, the minimum input voltage can be determined as.

$$V_{in}^{min} = \sqrt{{V_{OPFC}}^2 - \frac{2P_{in}T_H}{C_{DC-LINK}}} \quad (2.12)$$

Using (12) minimum input voltage is calculated as:

$$V_{in}^{min} = \sqrt{420^2 - \frac{2 \times 725 \times 20 \times 10^{-3}}{470 \times 10^{-6}}} = 340\ V \quad (2.13)$$

Min and Max Voltage Gain:

The LLC resonant converter is considered to execute at resonance frequency f_r for the nominal PFC output voltage. Considering the gain at resonance frequency as the minimum gain for the converter.

$$M^{min} = 1\ at\ f_s = f_r \quad (2.14)$$

The maximum voltage can be determined as:

$$M^{max} = \frac{V_{in}^{max}}{V_{in}^{min}} M^{min} = \frac{420}{349} \times 1 = 1.21 \quad (2.15)$$

Transformer Turns Ratio (n):

Using the minimum gain (M^{min}) turns ratio of the transformer is specified as:

$$n = \frac{N_p}{N_s} = \frac{V_{in}^{max}}{2(V_0 + V_X)} . M^{min} \quad (2.16)$$

Considering the voltage drop across the full bridge rectifier (V_X) equal to 0.8V, the turn ratio can be worked out as

$$n = \frac{V_{in}^{max}}{2(V_0 + V_X)} . M^{min} = \frac{420 \times (1)}{2(58 + 0.8)} = 3.6 \quad (2.17)$$

Equivalent Load Resistance (R_{ac}):

$$R_{ac} = \frac{8n^2}{\pi^2} \frac{V_0^2}{P_0} = \frac{8 \times 3.6^2}{\pi^2} \frac{58^2}{696} = 50.83\Omega \quad (2.18)$$

Resonant Network Parameters:

For computing resonant network parameters, the peak gain characteristics as given in [10] is used to determine proper quality factor (Q) and inductance ratio (m). It is noted that the higher peak gain can be obtained by reducing the Q and m values. The smaller the m value is smaller the magnetizing inductance value, which result in poor coupling of transformer, high circulating current and deteriorates the efficiency. Considering zero voltage switching and load transients, additional 10~20 % margin in peak gain is considered to determine proper Q value.

After determining the Q value, the resonant network components parameters are calculated as follows:

$$C_r = \frac{1}{2\pi Q f_r R_{ac}} \tag{2.19}$$

$$L_r = \frac{1}{(2\pi f_r)^2 C_r} \tag{2.20}$$

$$L_m = m \times L_r \tag{2.21}$$

M^{max} for the minimum input voltage (V_{in}^{min}) is 1.28. With a 15% margin, a maximum gain of 1.47 is needed. With inductance ratio(m) set to 5, Q is calculated as 0.4 using the peak gain curves shown in Fig.2.4. The resonant components for the resonant frequency(f_r) of 100 kHz are.

$$C_r = \frac{1}{2\pi \times 0.4 \times 100 \times 10^3 \times 50.83} = 78.31nF \tag{2.22}$$

$$L_r = \frac{1}{(2\pi \times 100 \times 10^3)^2 \times 78.31 \times 10^{-9}} = 32.38\mu H \tag{2.23}$$

$$L_m = 5 \times 32.38\mu H = 162\mu H \tag{2.24}$$

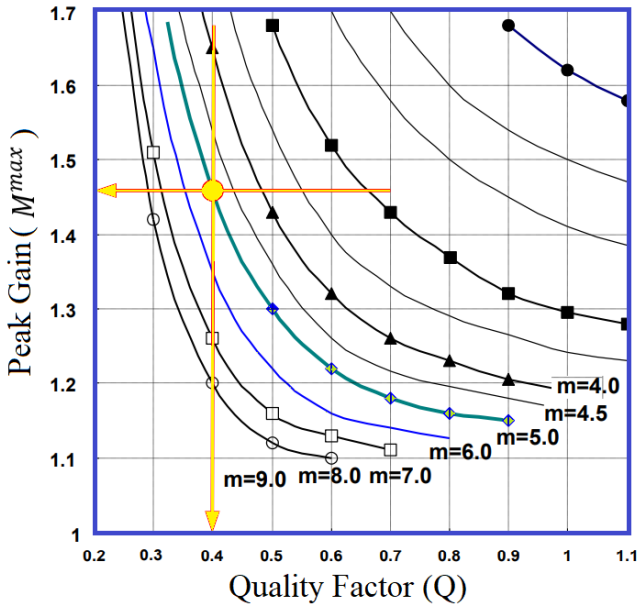

Fig. 2.4 Peak Gain characteristics w.r.t. Q for various m value

Minimum normalized frequency:

Differentiating the gain (M) of (2.8) in respect of F_X and equating to zero, minimum frequency is derived as,

$$\frac{dM}{dF_X} = 0 \Rightarrow F_X = 0.51 \tag{2.25}$$

$$f_{min} = F_x \times f_r = 0.51 \times 100 \times 10^3 = 51kHz \tag{2.26}$$

Estimated Currents in the converters:

Considering transformer overloading of 110 %, the RMS load current on the primary side is calculated as:

$$I_{op} = 1.11\frac{I_0}{n} = \frac{1.11 \times 12 \times 110}{100 \times 3.6} = 4.07\ A \tag{2.27}$$

Where I_0 is the output current and I_{op} is the load current on primary side of the transformer.

The RMS magnetizing current (I_m) for the minimum frequency 51kHz is

$$I_m = 0.9\frac{nV_0}{\omega L_m} \tag{2.28}$$

where, $\omega = 2\pi f_s$

$$I_m = \frac{0.9 \times 3.6 \times 58}{2\pi \times 51 \times 10^3 \times 162 \times 10^{-6}} = 3\ .6A \tag{2.29}$$

The resonant current I_p can be calculated as:

$$I_p = \sqrt{I_{op}^2 + I_m^2} = \sqrt{(4.07)^2 + (3.6)^2} = 5.45\ A \tag{2.30}$$

Referring primary current as $I_{op,}$ the secondary side transformer current (I_{os})

$$I_{os} = n \times I_{op} = 3.6 \times 4.07 = 14.64\ A \tag{2.31}$$

Selection of MOSFET Rating:

The Maximum rated voltage as commercially available is about 500 V. The same device is used in the simulation and the input voltage is varied from 340 V- 420V.

$$V_{Q1(peak)} = 340V\text{- }420\ V \tag{2.32}$$

The maximum current rating of MOSFET switch can be

$$I_{Q1\ (RMS)} = 6\ A \tag{2.33}$$

However, MOSFET of Fairchild FDPF12N50UT with rating of 500V/10A can be used for LLC experiment.

Selection of Rectifier Diode Rating:

Voltage Rating can be calculated as:

$$V_{DIODE} = \frac{\frac{V_{in}^{max}}{2}}{n} \times 2 = \frac{2 \times 420}{2 \times 3.6} = 116.66\,V \tag{2.34}$$

Current Rating can be determined as

$$I_{DIODE} = \frac{\sqrt{2} \times I_{os}}{\pi} = \frac{\sqrt{2} \times 14.64}{\pi} = 6.6\,A \tag{2.35}$$

Schottky Barrier Diode RB088T150NZ of ROHMS Semiconductor with rating 150V/10A can be used for LLC experiment.

Selection of Capacitive Output filter:

The RMS current of output capacitor at frequency of 100kHz for the load current $I_{0.}$

$$I_{C0} = I_0 \sqrt{\left(\frac{\pi^2}{8} - 1\right)} = 0.48 I_0 \tag{2.36}$$

$$I_{C0} = 0.48\,X\,12 = 5.78\,A \tag{2.37}$$

For battery charging, DC voltage ripple should be significantly low. Assuming 60mV output voltage ripple, the maximum series resistance (ESR_{max}) should be.

$$ESR_{max} = \frac{V_{oripple}}{\left(\frac{\pi}{2} I_0\right)} = \frac{0.06}{\frac{\pi}{2} \times 12} = 3.18 m\Omega \tag{2.38}$$

The output capacitive filter can be any value with the following requirements.

- ESR value should be less than 3.18 $m\Omega$.
- Ripple current rating should be 5.78A at frequency of 100kHz.
- Voltage rating should be 58 V

In the simulation 200 μF Capacitance value is used.

2.5 PI controller for LLC resonant converter

2.5.1 Closed Loop Control

Fig. 2.5 shows the negative feedback close loop LLC control circuit. The output voltage (V_o) of the resonant converter is compared with the reference voltage (V_{ref}) which gives the voltage error (V_{error}). The voltage error is managed by the Proportional-Integral (PI) controller to generate the control frequency signal. Finally, the control frequency signal is converted into pulse using PFM controller.

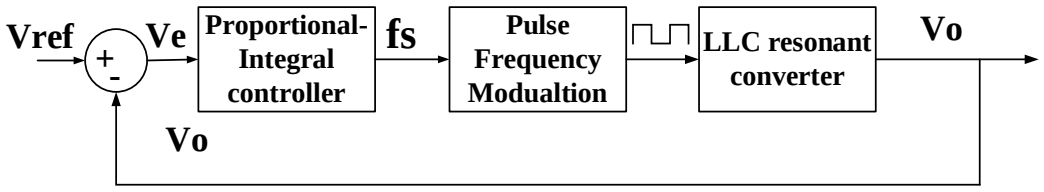

Fig. 2.5 Close loop of LLC resonant converter

2.5.2 Proportional-Integral (PI) Controller

The PI controller is depicted in Fig.2.6. The transfer function (G_{PI}) of the PI controller is given as:

$$G_{PI} = \frac{K_p(s) + K_i}{s} \tag{2.39}$$

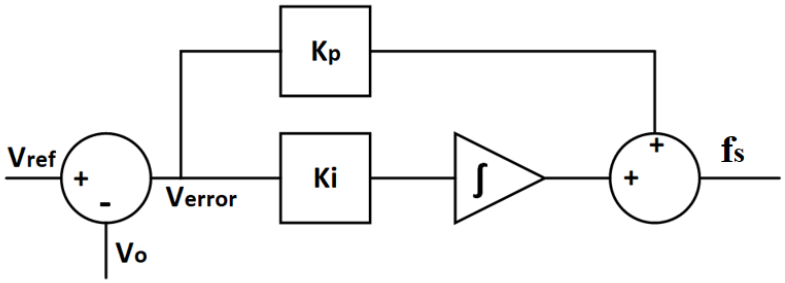

Fig. 2.6 PI controller

Where K_i is an integral gain and K_p is a proportional gain.

The gain values K_p =500 and $K_i = 5 \times 10^6$ has been determined by trial-and-error technique to obtain the desired output voltage.

2.5.3 Pulse Frequency Modulation (PFM)

The block diagram of PFM is shown in Fig.2.7 which is used in simulation to generate gate pulses for Q_1 and Q_2 interchangeably. The PFM changes the frequency for fixed duty cycle of 50 %.

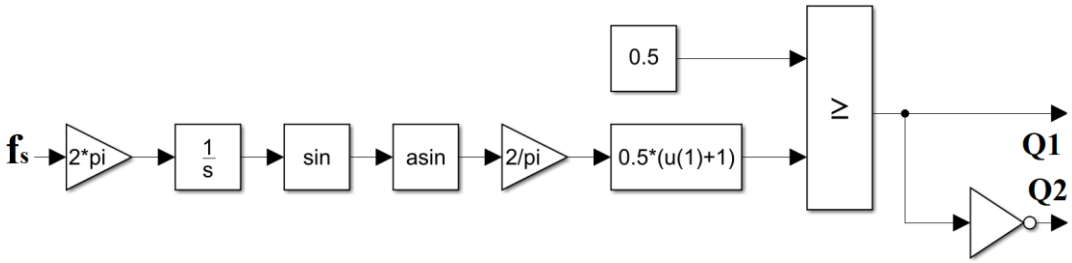

Fig. 2.7 PFM Controller

All the design parameters as calculated are summarized in Table 2.2.

Table 2.2 Design Parameters

Parameters	Designator	Value
Input Voltage	$V_{in\ min}$ -$V_{in\ max}$	340V - 420V
Output Voltage (Rated)	V_o	58V
Output Current (Rated)	I_o	12A
Output Power (Rated)	P_o	696 Watts
Resonant Frequency	f_r	100 kHz
Minimum switching frequency	f_{min}	51kHz
Turns Ratio	n	3.6
Magnetizing Inductor	L_m	162 μH
Resonant Inductor	L_r	32.38 μH
Resonant Capacitor	C_r	78.31nF
Capacitive filter	C_o	100 μF
Quality Factor	Q	0.4
Inductance ratio	m	5
Proportional Gain	K_p	500
Integral Gain	K_i	5×10^6

2.6 Simulation Results

Fig. 2.8 depicts the Simulink model of the LLC Resonant DC-DC Converter circuit. The output voltage is controlled with the help of PI controller. The simulation studies are carried out for the specific three modes of operation i.e., resonance mode, boost mode and buck mode.

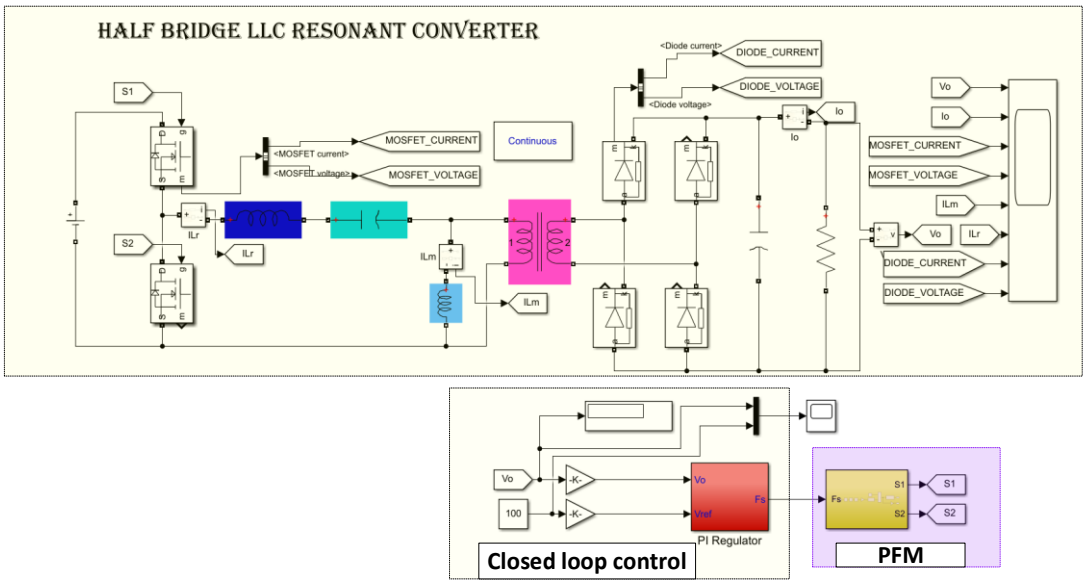

Fig.2.8 Simulink model of LLC resonant converter

The Gain (M) characteristics curve with respect to normalized frequency is plotted in Fig. 2.9 for and different values Q at m equal to 5.

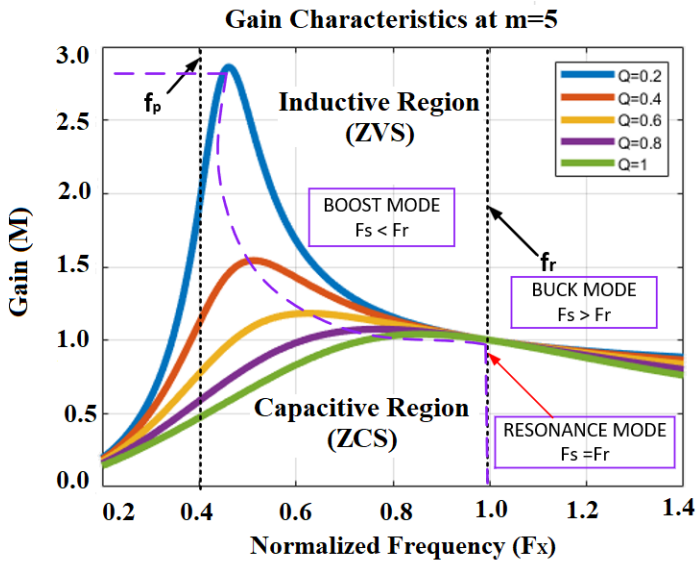

Fig. 2.9 Gain (M) characteristics for various quality factor (Q)

From Fig. 2.9 it can be observed that the gain at resonant frequency is unity and the operation at this point is considered as resonance mode of operation. For switching frequency less than the resonant frequency, the gain of the converter is greater than 1 and operation in this region is considered as boost mode operation up to certain switching frequency. For switching frequency greater than resonant frequency, the gain of the converter is less than 1 and operation in this region is buck mode operation. For optimal operation converter should be operated around the normalized frequency equal to1. The three mode of operation is simulated for the open loop by varying frequency.

2.6.1 Resonance Mode of Operation

Fig. 2.9 depicts the resonance mode operation indicating the normalized frequency is 1 i.e., $f_s=f_r$.

Fig.2.10 depicts the output voltage which is 57.7 V the ripple observed in the simulation is 120mV. The high value 57.70V and low value 57.58 V is measured. The gain of the converter is calculated by using equation 7 for input voltage 420 V, turns ratio 3.6 and obtained output voltage 57.7V is 1.

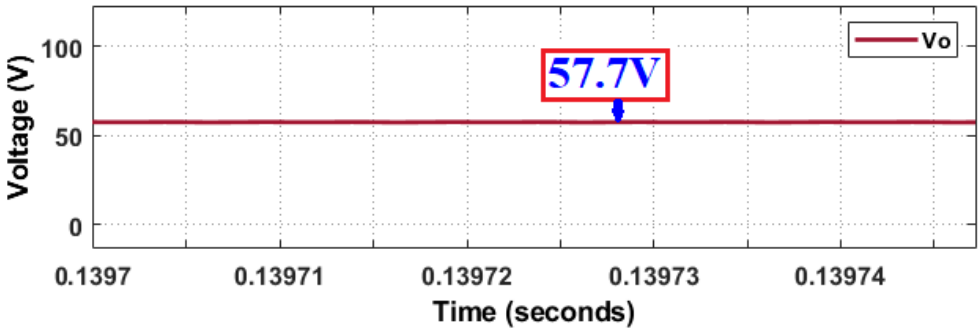

Fig 2.10 Output Voltage at resonance mode

The output current 11.8 A is shown in Fig. 2.11 which has ripple of 0.03 A. The high value 11.8 A and low value 11.5 A is measured from the simulation.

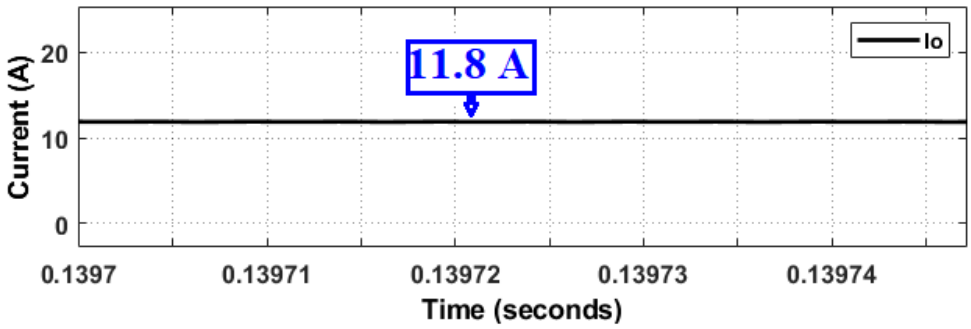

Fig 2.11 Output Current at resonance mode

In Fig.2.12 the resonant current and magnetizing current is shown. The RMS value of resonant current is 4.412 A is measured and RMS value of magnetizing current is 2.534 A is measured. From Fig.2.12, it can be observed that the resonant current is almost sinusoidal in nature.

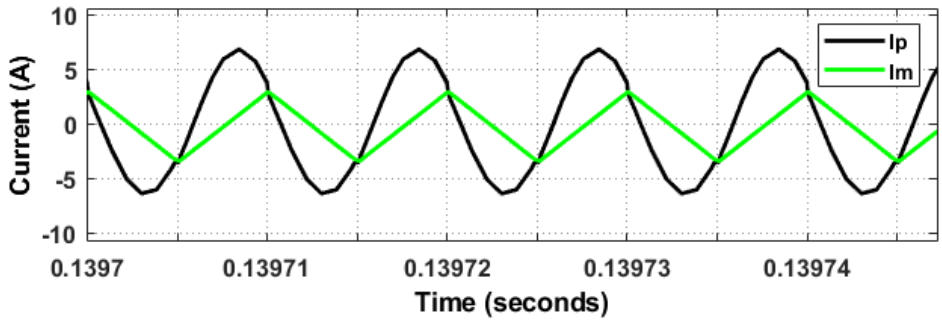

Fig. 2.12 Resonant and magnetizing current at resonance mode

Fig.2.13 shows the voltage across the resonant capacitor which is almost sinusoidal in nature. The peak value measured in simulation is 391.30 V.

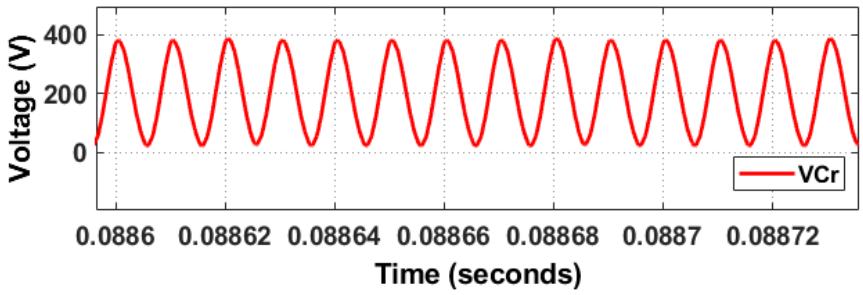

Fig. 2.13 Voltage across resonant capacitor at resonance mode

In Fig.2.14 the voltage across the Switching device Q_1 is shown. The peak voltage across the Q_1 is 420 V which is the input voltage applied to the converter. Resonant current also shown in Fig.2.12 to demonstrate the Zero Voltage Switching (ZVS). The resonant current is scaled by gain 20.

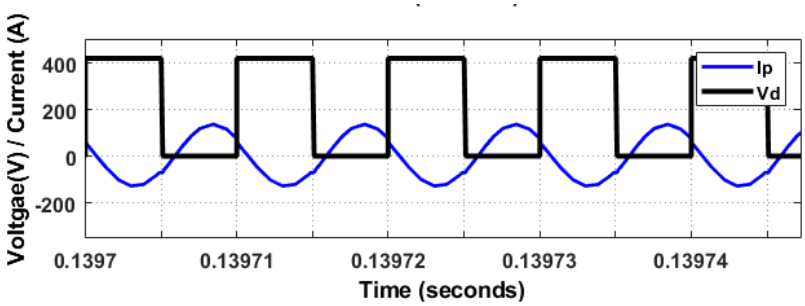

Fig.2.14 Voltage across MOSFET and resonant current in resonance mode

2.6.2 Boost Mode of Operation:

The switching frequency f_s = 80kHz is used to demonstrate the simulation results for boost mode (f_s<f_r). The expected gain at 80 kHz is 1.17 as shown in Fig. 2.15.

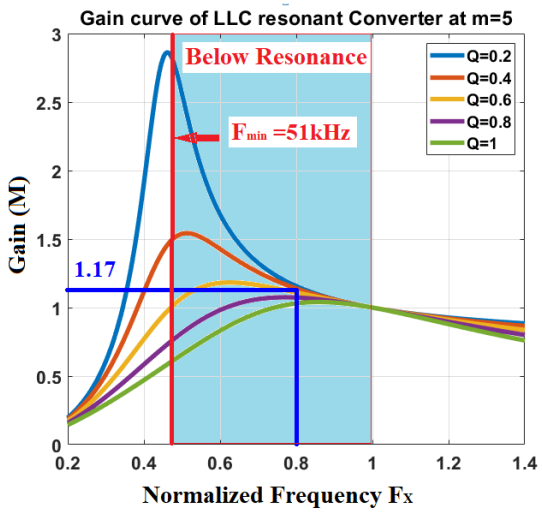

Fig.2.15 Boost mode operation

Fig.2.16 depicts the output voltage 68.30 V for the input voltage 420 V. The Gain can be calculate using (7). The Gain is 1.168 and ripple voltage measured is 0.35 V which higher than ripple observed at resonant mode, and the output voltage lies at 68.30 V (high) and 67.95 V (low).

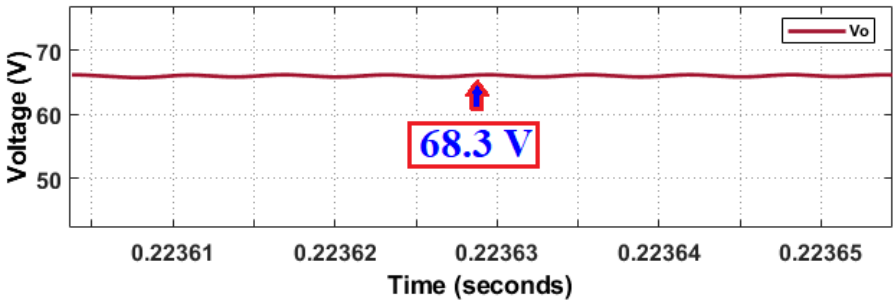

Fig.2.16 Output voltage for Boost Mode

The output current 13.70 A is measured from the simulation for this case. The ripple current is 0.1 A which is also higher than the ripple observed in the resonance mode.

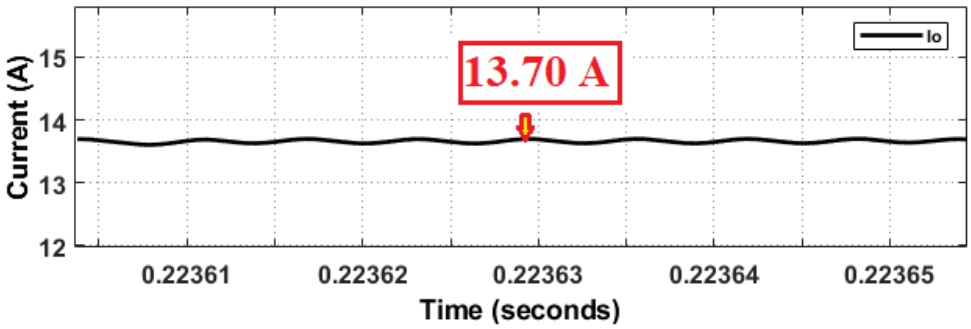

Fig. 2.17 Ouput Current for Boost Mode

The peak value of resonant current and magnetizing current is high in comparison of currents in resonance mode which increases the primary side conduction losses.

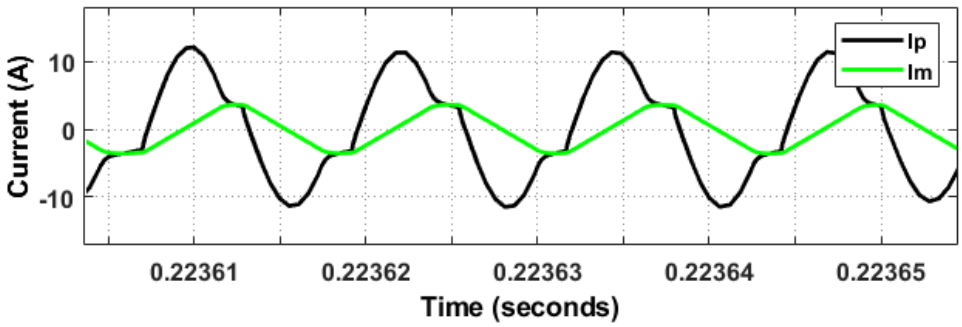

Fig. 2.18 Resonant and Magnetizing current for Boost Mode

The peak voltage across the resonant capacitor measured is 462.5 V and nature for the voltage is not purely sinusoidal as shown in Fig.2.19

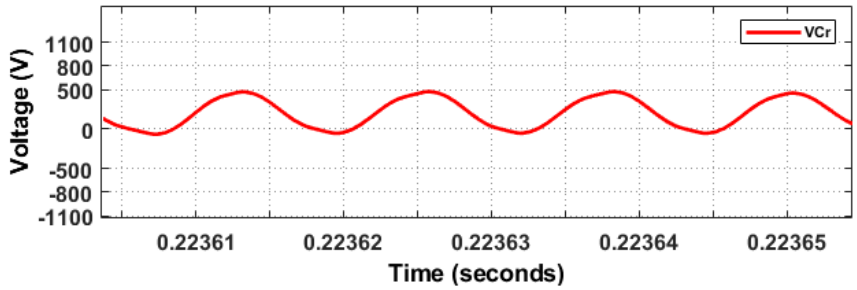

Fig. 2.19 Voltage across resonant capacitor for Boost Mode

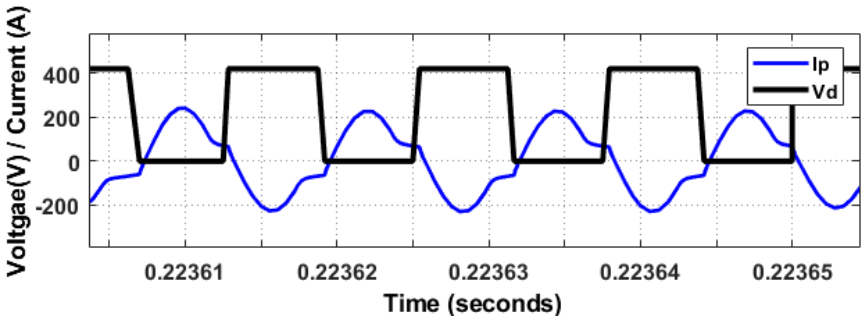

Fig.2.20 Voltage across MOSFET and resonant current in Boost Mode

In Fig. 2.20 The across Q_1 is shown with the peak voltage of 420 V. ZVS is achieved can be observed from the Fig.2.20**.** The Resonant current is scaled by the gain of 20.

2.6.3 Buck Mode of Operation

The switching frequency 120kHz is used to simulate the DC-DC converter for Buck mode ($f_s > f_r$). The expected gain for the buck mode is 0.88 as shown in fig.2.21.

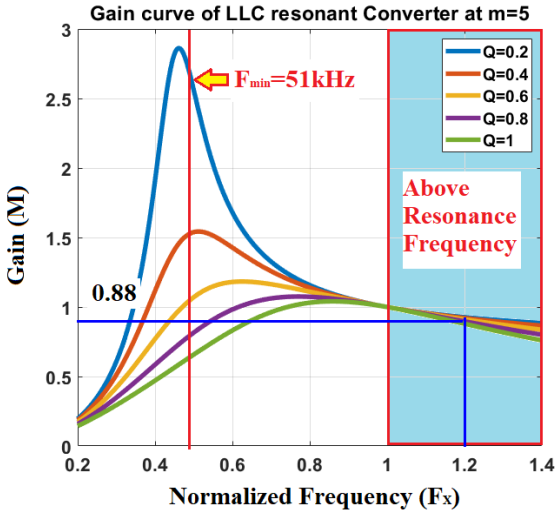

Fig.2.21 Buck mode operation

The output voltage is 51.72V as given in Fig.2.22 and ripple voltage of 0.1V is observed. The high value is 51.72V and low value is 51.62V. The gain is calculated using the (7) is 0.886.

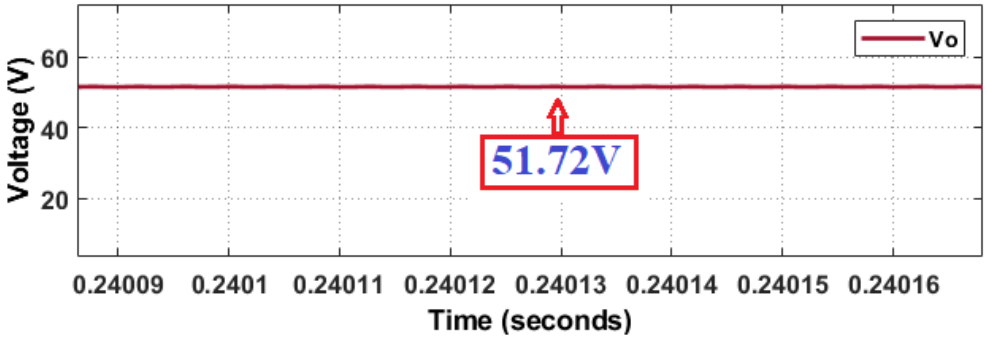

Fig.2.22 Output Voltage for Buck Mode

The output current 10.70A is observed at frequency 120kHz and current ripple 0.05A as shown in Fig.2.23.

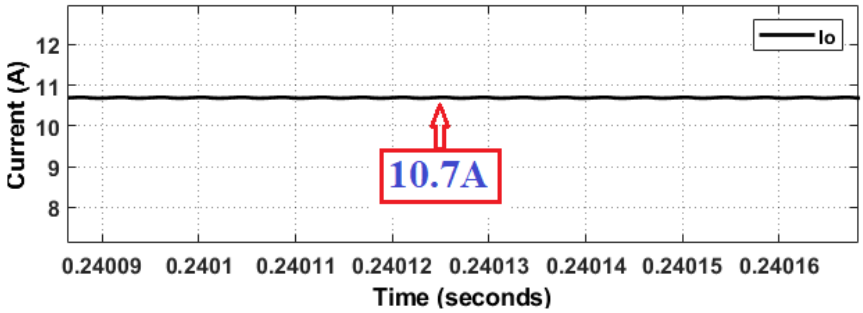

Fig.2.23 Output Current for Buck Mode

The RMS value of resonant current (I_p) is 4.05 A and RMS value of magnetizing current (I_m) is 1.833A.

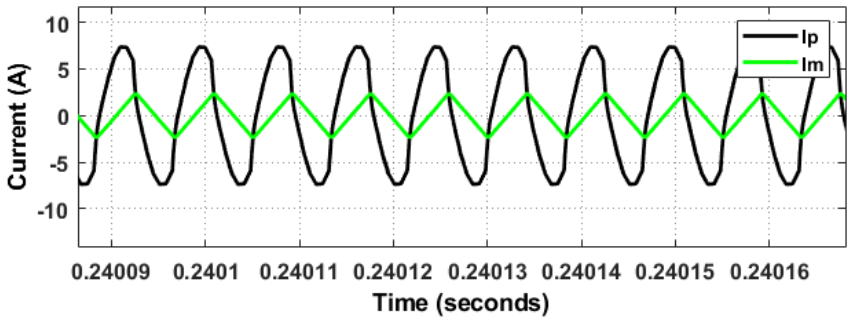

Fig.2.24 Resonant and Magnetizing current for Buck Mode

The voltage across the capacitor is shown in Fig.2.25 The peak voltage of 341.4 V is observed.

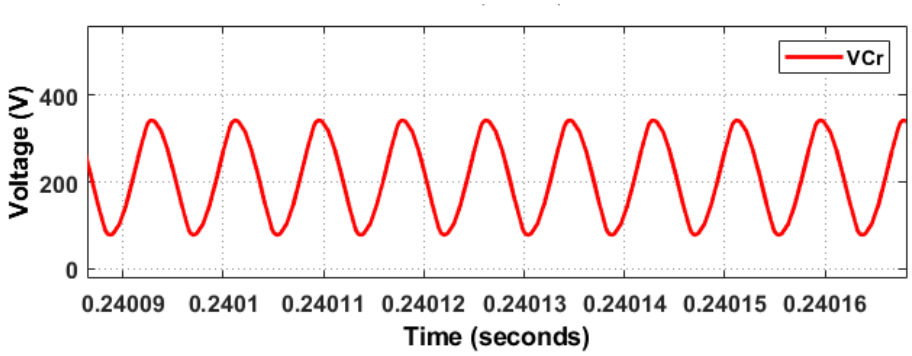

Fig.2.25 Voltage across resonant capacitor in Buck Mode

The peak value of V_d is 420 V and zero voltage switching is achieved as shown in the Fig. 2.26.

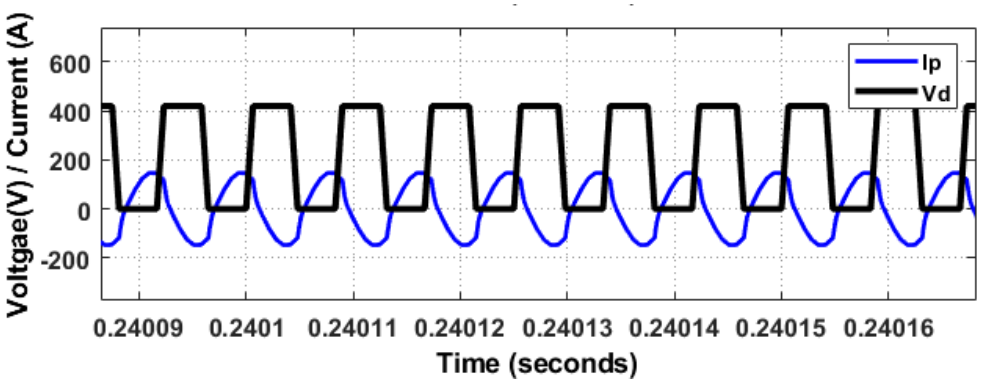

Fig. 2.26 Voltage across MOSFET and resonant current in Buck Mode

In all the three modes of operation, the best performance is observed at the resonance mode. To charge the battery switching frequency near the resonance frequency is established to be most suitable.

2.6.4 Verification of Input Voltage

The simulation is executed for various input voltage ranging from 340V to 420V. The PI- controller is used to keep output voltage at 58V. Fig.2.27 shows that the output voltage is well controlled for the varied input voltage.

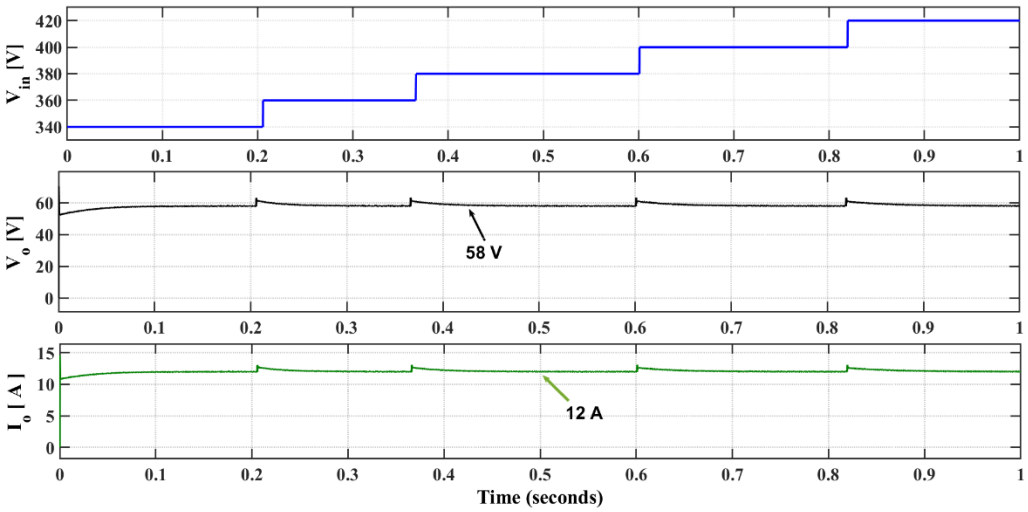

Fig. 2.27 Regulated output voltage and output current for wide input voltage

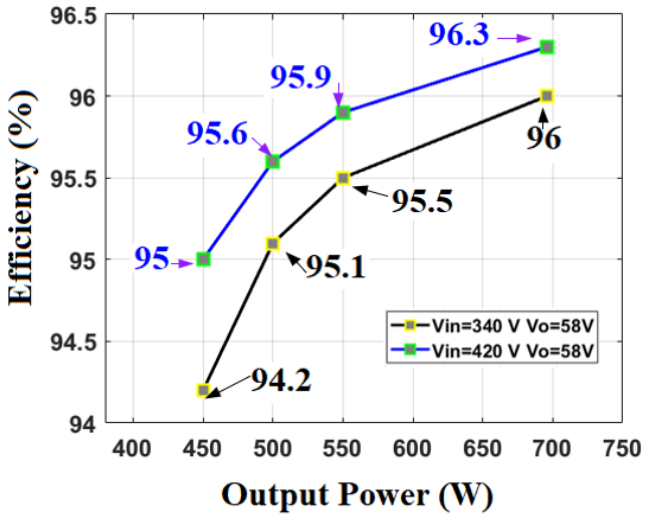

Fig. 2.28 Efficiency of converter at varying power output for different input voltages

Fig.2.28 shows the efficiency variation of the converter for maximum and minimum input voltage at different output power and constant output voltage 58V. The peak efficiency of 96.3 % is achieved for rated output power 696W at rated input voltage 420 V. At input voltage 340V the peak efficiency 96 % is achieved for rated output power.

2.7 Outcome of Proposed Work

In this chapter a high efficiency LLC Resonant Converter for battery charging application has been designed and its performances at resonance mode buck mode and boost mode of operations are validated through the simulation exercises done on MATLAB/ Simulink platform. The inductance ratio (m) and the Quality factor (Q) have

been identified to design the resonant converter of higher efficiency for battery charging application. The output voltage has been well regulated near the desired value of 58V for wide variation of input voltage 340V-420V. But, the variation in efficiency of the converter has been found to be marginal. However, the peak efficiency of 96.3 % has been achieved for rated input voltage of 420V and rated output voltage of 58V.

CHAPTER 3

BOOST CONVERTR AIDED LLC RESONANT CONVERTER

3.1 Introduction

A two-stage topology for battery charging is discussed. The first stage consists of diode bridge rectifier with boost converter for power factor correction. The control algorithm for boost converter in Discontinuous Conduction Mode (DCM) of input current although, make simpler the control algorithm of PFC but it suffers from high input current peak resulting in overdesign of input filters [64],[65]. This restricts the use of devices with lower power ratings. To overcome, Continuous Conduction Mode (CCM) of the input inductor current is used which reduces the input current stress for current shaping. The second stage is Half-Bridge Inductor-Inductor Capacitor (LLC) resonant DC-DC converter which facilitates the battery charging. The output voltage of the battery is controlled with the Proportional-Integral (PI) controller followed by Pulse Frequency Modulation (PFM) techniques. Operation and Control of Boost Converter Fed LLC Resonant Converter

A battery charger for an electric vehicle is depicted in fig.3.1 which used a boost converter as a front-end DC-DC converter and the second stage has Half-Bridge LLC resonant converter. The AC main supply has been given to the front-end boost converter through the Diode Bridge Rectifier (DBR). The PFC-Boost converter operates in Continuous Conduction Mode (CCM) of the input inductor current. The Active Power Factor Controller (APFC) is utilized to control the DC-link voltage and also to achieve harmonic free AC mains current. The APFC has a two-loop structure, the DC-link voltage feedback forms the outer voltage control loop and the input inductor current of the boost converter feedback is used to create the internal current control loop. The outer voltage control loop structure starts with the sensing voltage across the DC-link capacitor (V_d) which is compared with the reference DC-link voltage (V_d^*) and voltage error is generated. The voltage error is processed by the Proportional-Integral (PI) controller which gives the modulating current signal. Further, this modulating current signal is multiplied with a unit template of AC mains

voltage and the resultant signal is compared with the input inductor current of the boost converter to generate the current error signal which has been passed through the Proportional-Integral controller which acts as a current controller and resultant signal us compared with the saw-tooth carrier wave to produce the Pulse Width Modulating (PWM) switching pulses for the Boost converter switch.

Furthermore, The LLC resonant DC-DC converter builds the second stage. The DC-link voltage is fed to the LLC resonant converter and the output voltage of the converter is controlled with the PI-Controller. The output voltage (V_o) is compared with the reference output voltage (V_o^*) and processed through the PI-controller which acts as a voltage controller and the resultant signal is processed by the Pulse Frequency Modulation (PFM) controller which generates the switching pulse for the Half-Bridge LLC resonant converter.

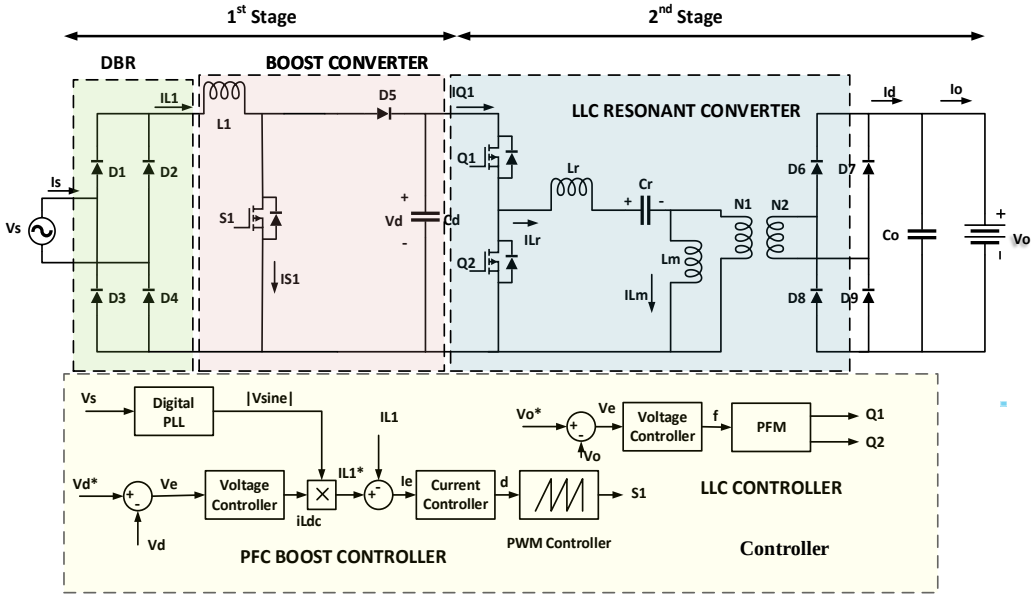

Fig 3.1 PFC-boost converter fed Half-Bridge LLC resonant converter

3.2 Design Parameters

The design parameters of an electric vehicle battery charger based on boost PFC are determined considering the following assumptions.

1. The semiconductor devices are ideal for this proposed topology.
2. The resistance load is considered for the battery.

3.2.1 Design of Power Factor Corrected Boost Converter

The design of the PFC based on boost converter is under the Continuous Conduction mode of input inductor using Active Power Factor Control (APFC). The design parameters are determined using the specification given in Table 3.1.

Table 3.1 Specification of Boost converter

Parameters	Variables	Values
Supply Voltage (AC Mains)	V_s	220V
Supply Frequency	f_{supply}	50 Hz
Output Power	P_o	576 W
Switching Frequency	f_{sw}	30kHz
Voltage ripple of DC-link Capacitor	ΔV_d	1.5 %
Current ripple of the input inductor	ΔI_{L1}	10%
DC-link Voltage	V_d	400 V

The duty cycle (D) is depending on the output voltage of the Diode Bridge Rectifier (DBR) (V_{dbr}) and DC-link voltage (V_d). Neglecting the voltage drop across the diode of DBR. The duty cycle can be expressed as,

$$D = \frac{V_d - V_{dbr}}{V_d} \tag{3.1}$$

The output voltage of DBR (V_{dbr}) for 220V supply voltage is 198V. The DC-link voltage 400V is considered for this design. So, the duty cycle is calculated as,

$$D = \frac{400 - 198}{400} = 0.50 \tag{3.2}$$

Considering 10% current ripple of the input current is calculated as,

$$\Delta I_{L1} = \frac{P_o}{V_{dbr}} \times 10\% = \frac{576}{198} \times 0.1 = 0.291\ A \tag{3.3}$$

The boost input inductor value is calculated considering ripple current 0.291A. The input inductor value is given as,

$$L_1 = \frac{V_{dbr} \times D}{\Delta I_{L1} \times f_{sw}} = \frac{198 \times 0.50}{0.29 \times 30 \times 10^3} = 11.37\ mH \tag{3.4}$$

To avoid high ripple at DC-link the voltage ripple is taken 1.5 percent of the DC-link voltage (V_d). The voltage ripple of DC-link voltage is expressed as,

$$\Delta V_d = \frac{1.5}{100} \times V_d = \frac{1.5 \times 400}{100} = 6V \tag{3.5}$$

Using voltage ripple 6V, the DC-link capacitor is expressed as,

$$C_d = \frac{P_o}{4\pi f_{supply} V_d \Delta V_{Cd}} = \frac{576}{4\pi \times 50 \times 400 \times 6} = 383\mu F \tag{3.6}$$

3.2.2 Design of Half-Bridge LLC Resonant Converter

The DC-link voltage (V_d) is well controlled by the voltage controller used in Active Power Factor Control as an outer loop. This DC-link voltage is applied to the second stage i.e., Half-Bridge LLC resonant converter. The design values of components of an LLC resonant converter are determined based on the specification given in Table 3.2.

Table 3.2 Specifications of Half-Bridge LLC

Parameters	Variables	Values
DC-link Voltage	V_d	400V
Output Voltage	V_o	48V
Output Power	P_o	576W
Resonant Frequency	f_r	70kHz

The turns ratio (T) for charge voltage of the battery 48V and DC-link voltage 400V is given as,

$$T = \frac{V_d}{2V_o} = \frac{400}{2 \times 48} = 4.16 \tag{3.7}$$

For operating the LLC resonant converter below resonance frequency, the turns ratio of the transformer 4.3 is selected. The peak current of the resonant tank of the LLC is calculated as,

$$I_{Lr} = \frac{2\pi P_o}{2V_d} = \frac{2\pi \times 576}{2 \times 400} = 4.52\ A \tag{3.8}$$

The resonant frequency 70kHz is selected for designing the parameters of a Half-Bridge LLC resonant DC-DC converter. The value of the resonant capacitor can be expressed as,

$$C_r = \frac{I_{Lr}}{2\pi f_r \, V_d/2} = \frac{4.52}{2\pi \times 70 \times 10^3 \times 400/2} = 51.4nF \tag{3.9}$$

To provide the suitable voltage gain for the LLC converter, the ratio of L_r and L_m is selected as 0.167. The value of resonant inductor and magnetizing inductance can be calculated as,

$$L_r = \frac{1}{(2\pi f_r)^2 C_r} = \frac{1}{(2\pi \times 70 \times 10^3)^2 \times 51.4n} = 100.6\mu H \tag{3.10}$$

$$L_m = L_r/0.167 = 100.6\mu H/0.167 = 604\mu H \tag{3.11}$$

3.3 Control techniques

The Boost converter controller has two loop structure. The outer voltage loop is used to control the DC-link voltage V_d. The voltage error (v_e) generated on comparing with the reference DC-link voltage is processed by Proportional-Integral (PI) controller and its resultant is given by,

$$i_{Ldc}(z) = i_{Ldc}(z-1) + G_{pv}\{v_e(z) - v_e(z-1)\} + G_{pi}v_e(z) \qquad (3.12)$$

Where G_{pv} and G_{pi} are proportional gain and integral gain for the voltage controller.

The input voltage sine template is multiplied with voltage loop output to generate reference input inductor current is given as,

$$I_{L1}{}^{*}(z) = I_{L1}(z) \times v_{\sin e}(z) \qquad (3.13)$$

The current error (I_e) is passed through the PI controller and resultant is expressed as,

$$d(z) = d(z-1) + G_{pi}\{I_e(z) - I_e(z-1)\} + G_{ii}I_e(z) \qquad (3.14)$$

Where G_{pi} and G_{ii} are proportional gain and integral gain for the current controller.

The second stage is formed by LLC resonant converter which uses Pulse Frequency Modulation (PFM) and voltage controller. The voltage error (V_{oe}) generated on comparison of reference output voltage and the battery voltage is processed by the PI controller and output is expressed as,

$$f(z) = f(z-1) + G_{pllc}\{V_{oe}(z) - V_{oe}(z-1)\} + G_{illc}V_{oe}(z) \qquad (3.15)$$

Where G_{pllc} is the proportional gain & G_{illc} is the integral gain of Half-Bridge LLC resonant converter.

The proportional and integral gain for various controller is given in Table 3.3.

Table 3.3 PI gain values

Gains	Values
Proportional-Gain of Voltage Controller (G_{pv})	0.44
Integral-Gain of Voltage Controller (G_{pi})	21.77
Proportional-Gain of Current Controller (G_{pi})	7.00
Integral-Gain of Current Controller (G_{ii})	1300
Proportional-Gain of LLC Controller (G_{pllc})	500
Integral-Gain of LLC Controller (G_{illc})	10,000

3.4 Simulation Results

This section deals with performance of the proposed converter for electric vehicle battery charger. The dynamic and steady state performance of the proposed

charger is analyzed by varying the supply input voltage and load variation. All parameters calculated in section III is summarized in Table 3.4.

Table 3.4 Design Parameters

Parameters	Variables	Values
Supply Voltage (AC Mains)	V_s	220V
Supply Frequency	f_{supply}	50 Hz
Output Power	P_o	576 W
Switching Frequency	f_{sw}	30kHz
DC-link Capacitor	C_d	383 μF
Input inductor of Boost Converter	L_1	11.37mH
DC-link Voltage	V_d	400 V
Resonant frequency	f_r	70kHz
Resonant Capacitor	C_r	604 μF
Resonant Inductor	L_r	100.6 μH
Magnetizing inductor	L_m	604 μH

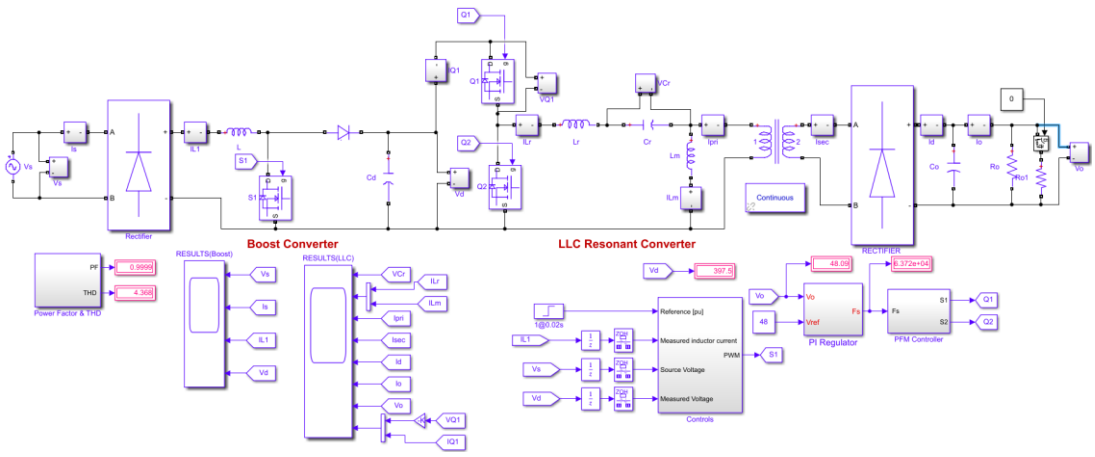

Fig. 3.2 Simulation block of PFC-boost fed Half-bridge LLC resonant converter

3.4.1 Steady-state performance of PFC-Boost converter

The steady-state behavior of the power factor corrected boost converter is analyzed for the supply voltage V_s = 220V and the DC-link voltage V_d = 400V. The battery voltage V_o = 48V for rated output power P_o = 576 Watts. The AC mains supply current I_s waveform is sinusoidal in nature with a peak amplitude of 4A. The input inductor

current I_{L1} is in continuous conduction mode and maximum values of current is reaches to 4A. The waveform of the I_{L1} is depicted in fig.3.3 The DC-link voltage V_d = 400V is achieved which is well regulated with the PI-controller.

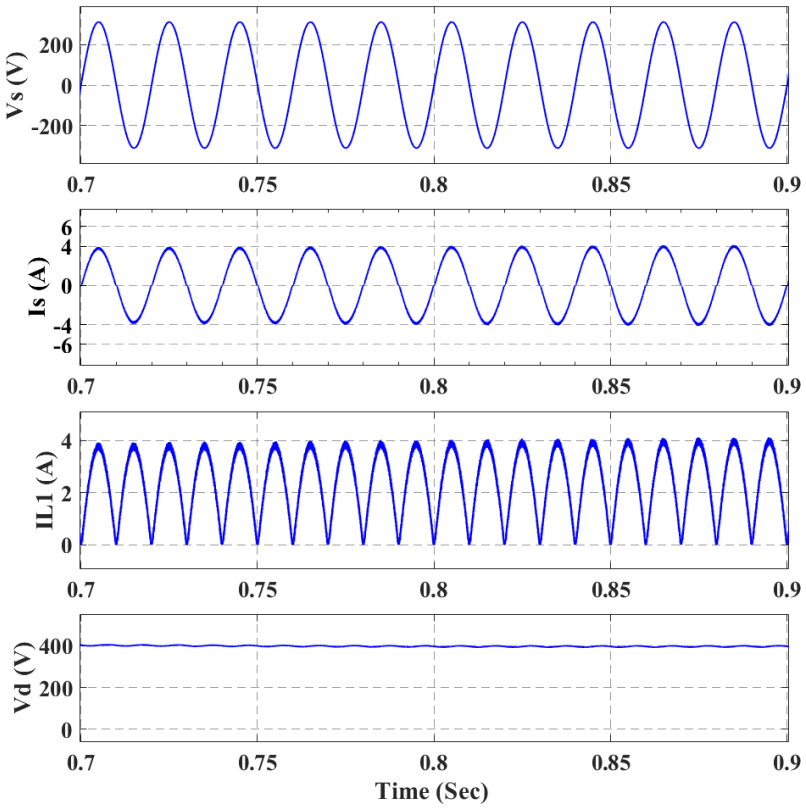

Fig. 3.3 Steady-state performance of supply current (I_s), input inductor current (I_{L1}) and DC-link voltage (V_d) at supply voltage (V_s) =220V.

3.4.2 Steady-state performance of LLC resonant converter

The steady-state performance of the Half-Bridge LLC resonant converter is discussed here. The battery voltage V_o = 48V is achieved with load current I_o = 12A. The peak amplitude of magnetizing current I_{Lm} is 1.2A shown in fig.3.4. with triangular current waveform and resonant current I_{Lr} has a peak value of 5.1A. The waveforms of I_{Lm} and I_{Lr} shows that the Half-Bridge LLC resonant converter is operating near the resonant frequency which is most appropriate region for optimal operation of the LLC resonant converter. The voltage across the capacitor V_{Cr} has maximum value of 404V for the load P_o =576 W. The rectifier output current I_d is in continuous current mode with the peak amplitude of 21A.

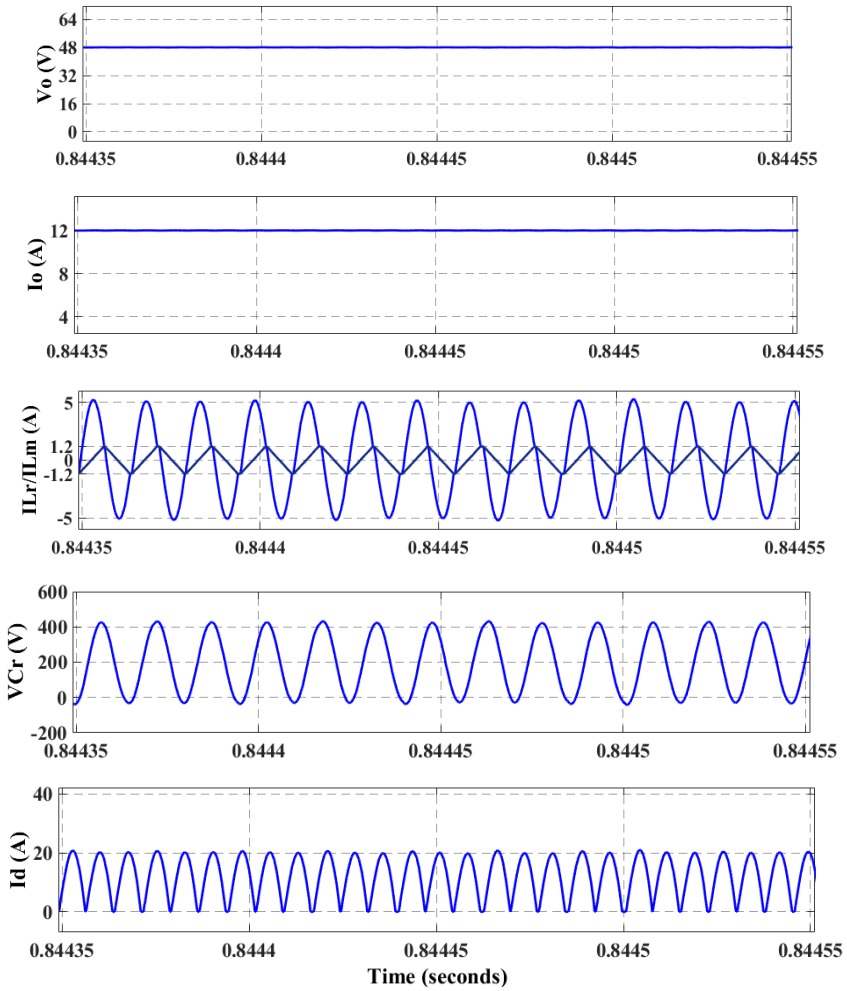

Fig. 3.4. Steady-state performance of battery voltage (V_o), battery current (I_o), resonant current (I_{Lr}), magnetizing current (I_{Lm}), resonant capacitor voltage (V_{Cr}) and rectifier current (I_d) at load (P_o)=576 W

3.4.3 Dynamic performance of PFC-Boost Converter

The dynamic performance of the PFC-Boost converter is depicted in fig.3.5 for various input voltage. For the analysis of dynamic behavior, the PFC-Boost is tested under various supply voltage from 185V to 265V. Initially, the supply voltage V_s = 185V was set which increase to 265V at time 0.6550 sec again reduced to 220V at 0.9 sec. The source current I_s decrease with increase of supply voltage and increase with decrease of supply voltage with harmonic free waveform can be observed from fig.3.5. The input inductor current I_{L1} is continuous conduction mode and peak current follows the AC mains supply peak current. The DC-link voltage V_d is dependent on supply voltage on increasing the supply voltage and decrease with decrease of supply voltage but settled to 400V as it is well regulated with the PI-controller.

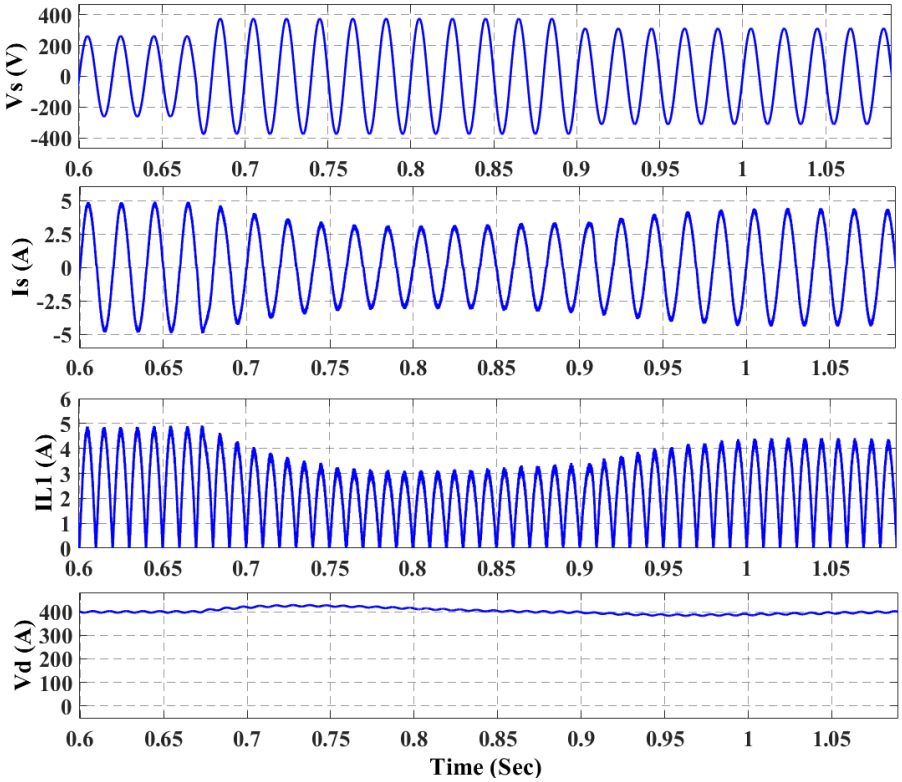

Fig.3.5. Dynamic performance of supply current (I_s), input inductor current (I_{L1}) and DC-link voltage (V_d) at various supply voltages

3.4.4 Dynamic performance of LLC resonant converter

The dynamic performance of Half-Bridge LLC resonant DC-DC converter is verified by varying the load P_o = 576W to P_o = 720 W. The output voltage remains constant which is well regulated with PI-controller. The load current I_o changes from 12A to 15A. The magnetizing current I_{Lm} remain constant to 1.2A but the resonant current increase with the increase of load can be observed from fig.3.6 and it also shows that the LLC resonant current is performing near resonant frequency which is best suitable point for optimal operation of LLC resonant current. The maximum voltage across resonant capacitor V_{Cr} initially at 400V but it increased with the increase of load. The peak amplitude value of rectifier output current I_d is increases up to 30A form 20 A and operating continuous conduction mode.

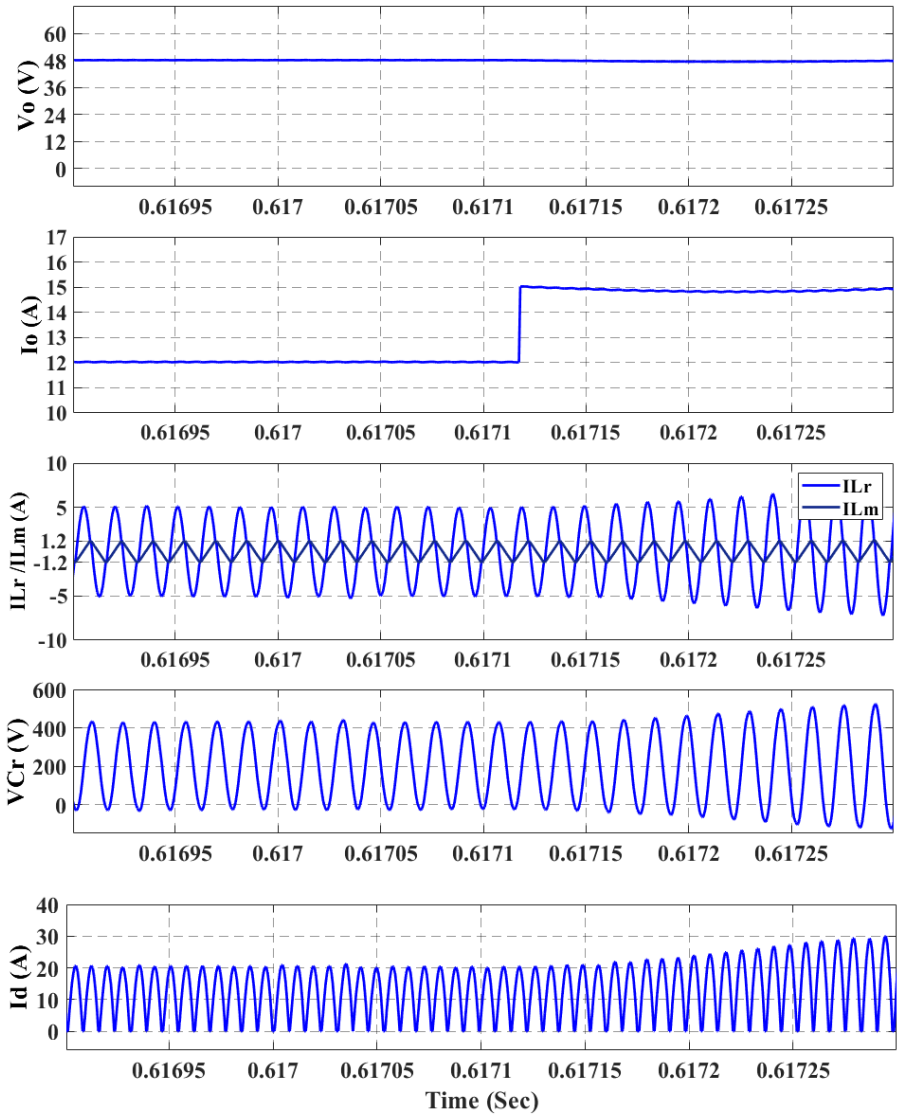

Fig.3.6. Dynamic performance of battery voltage (V_o), battery current (I_o), resonant current (I_{Lr}), magnetizing current (I_{Lm}), resonant capacitor voltage (V_{Cr}) and rectifier current (I_d) under different load.

3.4.5 Power Factor variation under different Input voltages

The proposed battery charger is tested under various AC mains supply voltage range from 150V to 260V and maximum Total Harmonic Distortion (THD) 3.18% is observed at high input voltage 260V with power factor PF = 0.99949 for the load P_o =576W. All the data for different input voltages and resultant power factors, AC mains supply current and THD at load 576 Watts are summarized in Table.3.5.

Table 3.5 Power Factor at different supply voltages

V_s (V)	I_s (A)	PF	THD (%)	P_o (W)
150	4.129	0.99962	2.75	576
160	3.877	0.99966	2.61	576
170	3.643	0.99969	2.48	576
180	3.441	0.99969	2.49	576
190	3.260	0.99971	2.39	576
200	3.097	0.99966	2.60	576
210	2.949	0.99968	2.52	576
220	2.815	0.99965	2.63	576
230	2.693	0.99964	2.70	576
240	2.581	0.99958	2.89	576
250	2.477	0.99953	3.07	576
260	2.382	0.99949	3.18	576

3.5 Outcome of Proposed Work

A power factor corrected Half-Bridge LLC resonant converter is designed for battery charging application in electric vehicles. Boost converter with active power factor controller is used to maintain sinusoidal input current. Steady-state and dynamic performance of the suggested topology has been tested under load variation and supply voltage variation. The power factor has been measured for different input voltage. An excellent performance has been observed with smooth sinusoidal input current

CHAPTER 4

SEPIC CONVERTR AIDED LLC RESONANT CONVERTER

4.1 Introduction

A two- stage on-board EV battery charger with SEPIC converter at the primary stage for power factor correction & Half-Bridge LLC resonant converter at the secondary stage to facilitate the battery charging is designed. The advantages of SEPIC over the boost converter are, it has the ability to perform the buck and boost operation as well as it eliminates the presence of inrush current. A variable DC-link voltage source is supplied to the HB-LLC which varies according to the battery voltage so that the resonant converter can function near the resonance frequency which reduces the high switching and circulating losses. Hence, the HB-LLC can attain higher efficiency for the entire range of the battery voltage. Consequently, improve the overall efficiency of the proposed charger specifically when the battery voltage is less than nominal battery voltage. The schematic diagram of the anticipated EV battery charger is depicted in Fig.4.1.

The unique features of the proposed EV battery charger are:

1. A unique technique is adopted to optimize the overall efficiency of the EVBC by operating near the resonant frequency.
2. It has the ability to perform wide input voltage ranges ($85V_{rms}$ - $220V_{rms}$) at unity power factor.
3. It also has the ability to charge the battery for a wide range of voltages (48V – 80 V) at high efficiency.
4. It gives excellent performance from light load to full load.

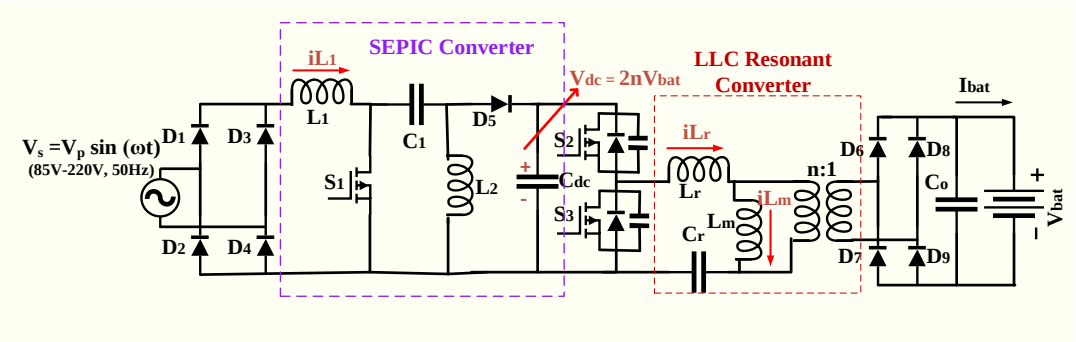

Fig. 4.1 The Schematic diagram of proposed charger EV battery charger is based on a PFC-SEPIC and HB-LLC resonant converter

4.2 Design of the PFC- SEPIC Converter

4.2.1 Overview of SEPIC Converter

The proposed configuration of PFC-SEPIC is working in the Continuous Conduction Mode (CCM) of the primary inductor current. In CCM, there are two modes in one cycle. The mode of operation of the SEPIC converter is depicted in Fig.4.2. The typical waveforms for line frequency and switching frequency are shown in Fig.4.3.

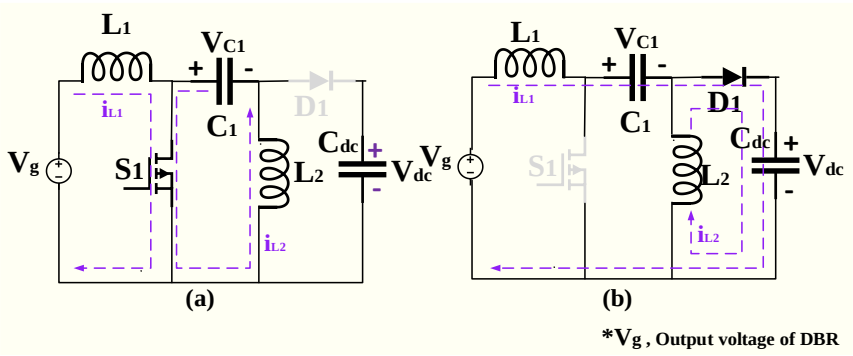

Fig. 4.2. Operation of SEPIC converter (a) Mode-1 (Switch-ON mode) (b) Mode -2 (Switch-OFF mode)

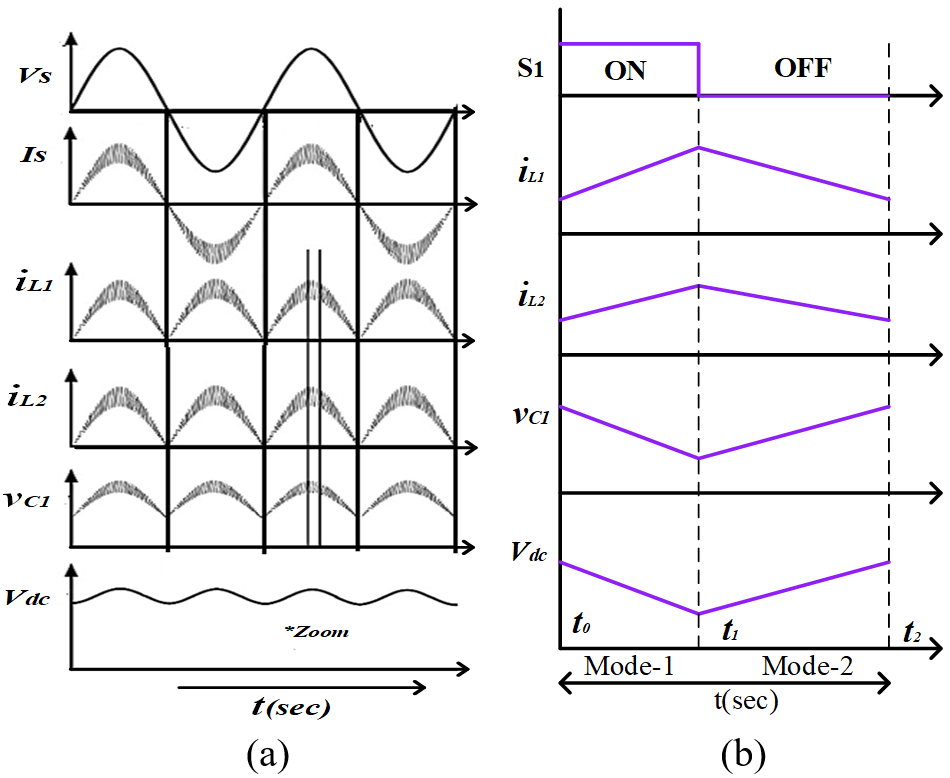

Fig.4.3. Typical waveforms of voltage and current across different components of SEPIC converter (a) Waveforms at line frequency (b) Waveforms at switching frequency

Mode of operation

Mode-1 (t_0-t_1): In this mode, the diode D_1 is in the reverse-biased mode, and switch S_1 is ON. Primary inductor L_1 stores the energy from the supply and the intermediate capacitor C_1 passes its stored energy to the secondary inductor L_2. For Fig.4.2. (a) it can be observed that the switch S_1 provides a shared path for the current flowing in two different meshes. The voltage across the DC-Link V_{dc} act as the source for the second stage LLC resonant converter.

Mode-2 (t_1-t_2): In this mode, the diode D_1 is in the forward-biased mode, and switch S_1 is turned OFF. At this time of interval, the intermediate capacitor starts charging through the primary inductor L_1. The DC-link capacitor C_{dc} is charged by both the primary and secondary inductor. The modes of operation are depicted in Fig.4.2. (b). The theoretical waveforms of the voltage and current of different components of the SEPIC converter for both modes are shown in Fig.4.3.

4.2.2 Computation of Design Parameters

Duty cycle

Ignoring the voltage ripple at the DC-link capacitor, the dc-link voltage can be assumed as constant voltage V_{dc}. So, the duty cycle is given as,

$$d(t) = \frac{V_{dc}}{V_P|\sin(\omega t)| + V_{dc}} \quad (4.1)$$

where, V_P is the amplitude of the line voltage, and ω is the angular line frequency, which is usually 100π rad/s in India.

The variation of the duty cycle of the SEPIC in steady state is describe in Eq. (4.1). The range of duty cycle is given as,

$$\frac{V_{dc}}{V_{savg} + V_{dc}} \leq d(t) \leq 1 \quad (4.2)$$

The average input supply voltage V_{savg} for nominal input voltage is calculated as,

$$V_{savg} = \frac{2\sqrt{2}V_s}{\pi} = \frac{2\sqrt{2} \times 220}{\pi} = 198V \quad (4.3)$$

For DC-link voltage V_{dc} = 300V and V_{savg} =198V, duty cycle is calculated using eq. (4.1) is 0.60.

Primary and Secondary Inductors L_1 and L_2

At high power level, CCM is preferred over the discontinuous conduction mode (DCM) since the current stress of the component is much smaller than DCM. Considering current ripple ΔI_{Li} the inductor value can be calculated as,

$$L_i = \frac{V_{savg} \times d}{\Delta I_{Li} \times f_{sw}} \quad (4.4)$$

Where, d is duty cycle, f_{sw} is a switching frequency of the SEPIC converter.

Considering current ripple 20% and switching frequency 50kHz, the inductor values L_1 and L_2 are calculated as 2.376mH.

Intermediate Capacitor C_1

The value of the intermediate capacitor C_1 with voltage ripple ΔV_{C1} is calculated as,

$$C_1 = \frac{P_o d}{V_{dc} \times f_{sw} \times \Delta V_{C1}} \quad (4.5)$$

Considering the voltage ripple 20% of the DC-link voltage, switching frequency 50kHz, output power P_o=1kW, dc-link voltage 300V and d =0.6. The intermediate capacitor C_1 is calculated as 667nF.

DC-Link Capacitor C_{dc}

The dc-link capacitor value with voltage ripple ΔV_{dc}, and supply frequency f_{supply} is calculated as,

$$C_{dc} = \frac{P_o}{4\pi f_{supply} V_{dc} \Delta V_{dc}} \tag{4.6}$$

In order to decrease the voltage ripple, a large value of capacitor is chosen. Though, this would make the capacitor large. The tradeoff between dc-link voltage ripple and capacitor size must be consider when designing the converter. Considering 1.5% dc-link voltage ripple the C_{dc} is calculated as 1180 μF.

4.3 Design of Half-Bridge LLC resonant converter

4.3.1 Overview of LLC resonant converter

The schematic diagram of Half-Bridge LLC resonant converter is depicted in Fig.4.4.

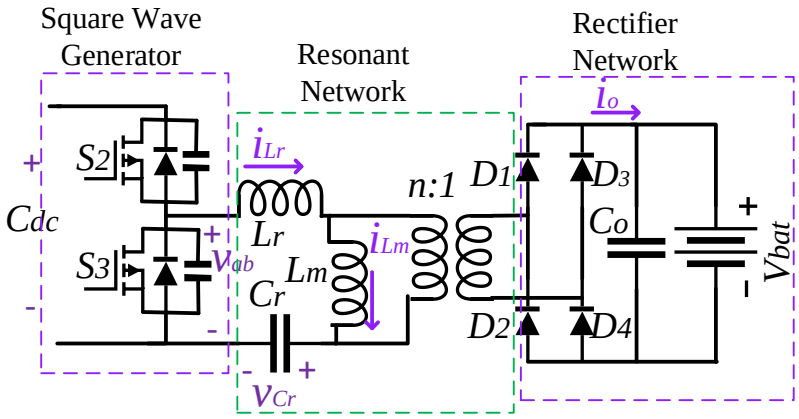

Fig.4.4 Schematic diagram of Half-Bridge LLC resonant converter

The non-sinusoidal configuration of the LLC resonant converter is depicted in Fig. 4.5 (a) and the linear sinusoidal configuration of the LLC resonant converter is depicted in Fig. 4.5 (b) which is based on First Harmonic Approximation (FHA) as explained in [62].

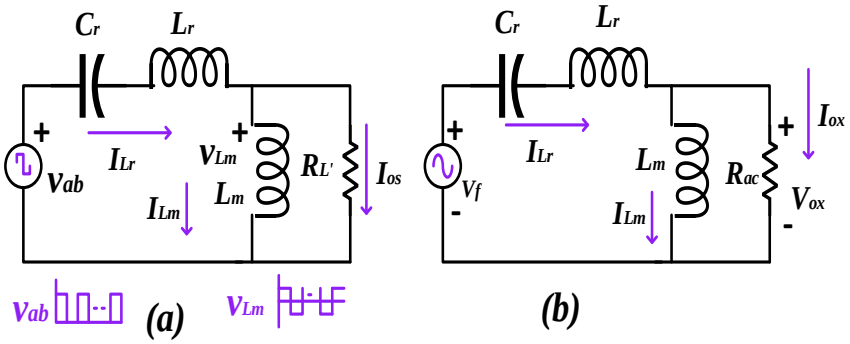

Fig.4.5 Modeling of HB-LLC resonant converter (a) Nonlinear sinusoidal configuration (b) Linear sinusoidal configuration.

The transfer function (M) of the LLC resonant converter can be obtained from the circuit configuration depicted in Fig. 4.5 (b)

$$M = \frac{V_{ox}(s)}{V_f(s)} \tag{4.7}$$

$$M = \frac{sL_m \,||\, R_{ac}}{(sL_m \,||\, R_{ac}) + sL_r + 1/sC_r} \tag{4.8}$$

Where V_{ox} is the primary input voltage and V_f is a fundamental voltage of v_{ab}.

The equivalent resistance R_{ac} and resonant frequency f_r can be given as:

$$R_{ac} = \frac{8V_{bat}}{\pi^2 i_0} \tag{4.9}$$

$$f_r = \frac{1}{2\pi\sqrt{L_r C_r}} \tag{4.10}$$

The fundament input voltage v_{ab} can be given as:

$$V_f(t) = \frac{2}{\pi} \times V_{dc} \times \sin(2\pi f_s t) \tag{4.11}$$

The root mean square (RMS) value of V_f is expressed as:

$$V_{frms} = \frac{\sqrt{2}}{\pi} V_{dc} \tag{4.12}$$

The fundamental voltage of v_{Lm} is given as V_{ox}:

$$V_{ox} = \frac{4n}{\pi} V_{bat} \times \sin(2\pi f_s t - \theta x) \tag{4.13}$$

Where n is the turns ratio of the transformer and θx is the phase angle between V_{ox} and V_f.

The RMS value of V_{ox} can be determined as:

$$V_{oxrms} = \frac{2\sqrt{2}}{\pi} \times n \times V_{bat} \tag{4.14}$$

The gain in terms of V_{dc} and V_{bat} can be determined by dividing (4.13) by (4.11).

$$M = \frac{V_{ox}}{V_f} = \frac{2nV_{bat}}{V_{dc}} \tag{4.15}$$

The magnitude of gain is:

$$M = \left| \frac{m \times {F_n}^2}{[(m+1) \times F_n^2 - 1] + j(F_n^2 - 1) \times F_n \times Q \times m} \right| \tag{4.16}$$

Regardless of load variation, the gain at the resonant frequency (f_r) remains constant:

$$M = \frac{2nV_{bat}}{V_{dc}} \; at \; f_s = f_r \tag{4.17}$$

Where $Q = \sqrt{L_r/L_m}/R_{ac}$ is quality factor, m is defined as L_r/L_m, f_s is the switching frequency of LLC and $F_n = f_s/f_r$. is the normalized frequency.

The gain variation with respect to frequency for various quality factor Q at single inductance ratio m is depicted in Fig.4.6. There are three operating mode such as resonance mode, boost mode and buck mode.

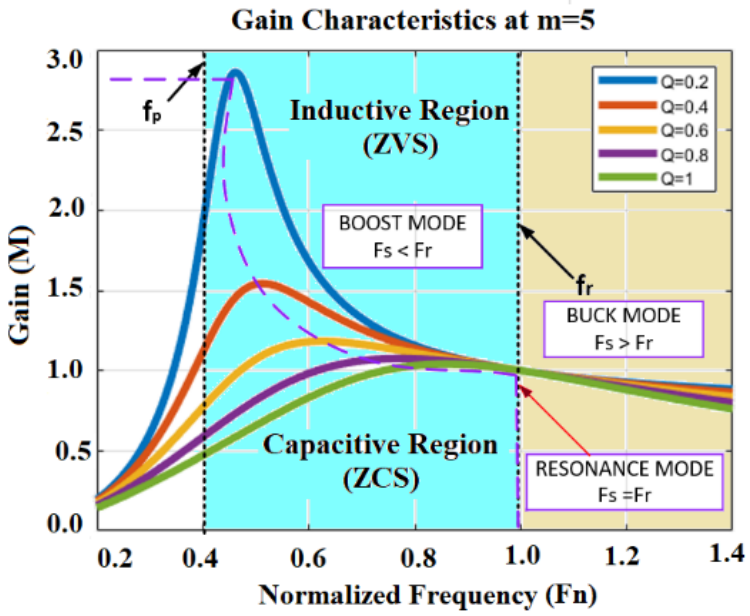

Fig.4.6. Gain (M) characteristics of LLC resonant converter for various Quality factor (Q) for single Inductance ratio (m) = 5.

4.3.2 Best operating point of LLC resonant converter

The waveforms of the resonant and magnetizing current are depicted in Fig.4.7. If operating frequency is lower than the resonance frequency depicted in Fig.4.7 (a), a high circulating current flow in the resonant network which causes high conduction losses. Fig.4.7 (b) shows the waveforms at operating frequency is equal to the resonant frequency, the switching and conduction loss are reduced. When the operating frequency is greater than the resonance frequency the MOSFET is turned off with high current as depicted in Fig.4.7 (c) which cause high switching loss. The performance of LLC resonant converter under various switching frequency is concluded in Table 4.1. It can be observed from the Table 4.1 that LLC resonant converter attain its best efficiency when it working at resonance frequency.

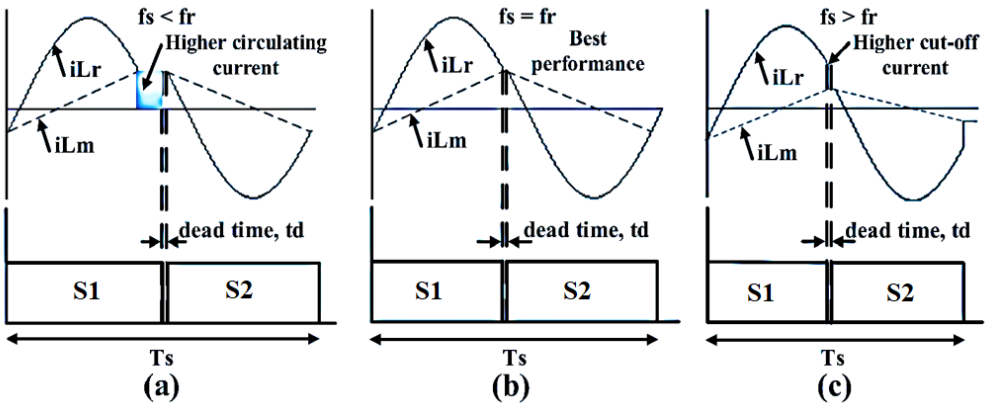

Fig.4.7 Waveforms of resonant current (i_{Lr}) and magnetizing current waveforms (i_{Lm}) for different operating point (a) $f_s < f_r$ (b) $f_s = f_r$ (c) $f_s > f_r$

Table 4.1 Performance of LLC resonant converter for various switching frequency

Performances	**$f_s < f_r$**	**$f_s = f_r$**	**$f_s > f_r$**
Turn on loss of MOSFET switch	ZVS	ZVS	ZVS
Turn off loss of MOSFET switch	Low	Low	High
Circulting current on primary side	High	Low	Medium
Secondary diodes	ZCS	ZCS	No
Conduction losses	High	Low	Medium
Switching losses	Low	Low	High
Harmonics	Low	Low	High
Overall Performance	Medium	Best	Medium

Where, f_r = 100kHz, and switching frequency f_s *is* [51kHz – 140Khz] is taken to estimate the performance given in Table.4.1.

4.3.3 Computation of Design parameters of Half-Bridge LLC

Turns ratio of the transformer

The regulated dc-link voltage is feed to HB-LLC resonant converter for EV battery charging. Considering nominal battery voltage V_{bat} = 57V and dc-link voltage V_{dc} = 300V. The turns ratio (n) of the transformer can be calculated as,

$$n = \frac{V_{dc}}{2V_{bat}} = \frac{300}{2 \times 57} = 2.63 \qquad (4.18)$$

Resonant Capacitor of LLC

The peak value of resonant current, I_{Lr} of the LLC resonant converter can be calculated as,

$$I_{Lr} = \frac{2\pi P_o}{2V_{dc}} = \frac{2\pi \times 1kW}{2 \times 300} = 10.46\ A \quad (4.19)$$

Considering resonance frequency f_r = 100kHz, the value of resonant capacitor is calculated as,

$$C_r = \frac{I_{Lr}}{2\pi f_r \, V_{dc}/2} \quad (4.20)$$

Using Eq. (4.20) the resonant capacitor is calculated as111nF.

Inductance Ratio, Resonant and Magnetizing Inductor

In order to select the inductance ratio (m), the smaller m value is reducing the size magnetizing inductance, which result in poor coupling of transformer, high circulating current and deteriorates the efficiency but provide higher gain, while with higher m value increase the size of magnetizing inductor, reduces the circulating current and improve the efficiency [11]. The inductance ratio in this work is chosen as m=5. The resonant capacitor and magnetizing inductance are determined using following equations,

$$L_r = \frac{1}{(2\pi f_r)^2 C_r} \quad (4.21)$$

$$L_m = mL_r \quad (4.22)$$

The values of resonant capacitor and magnetizing capacitor are calculated using Eq. (4.21) and (4.22) as, $22.8\mu H$ and $114\mu H$.

4.4 Control technique of the EV battery charger

In this work, the power factor correction is done with Active Power Factor Correction (APFC) which has two-loop structure. The outer loop is voltage control loop utilized to control the dc-link voltage. The reference dc-link voltage is generated by measuring the battery voltage so, $V^*_{dc} = 2nV_{bat}$. The dc-link voltage keeps varying according to the battery voltage. The dc-link voltage V_{dc} is compared with the reference V_{dc}* to generate the error voltage which is processed by the Proportional-Integral (PI) controller and its resultant is modulating current signal. This modulating current signal is multiplied by unit template of AC mains voltage and generate reference current for the primary inductor current. The primary inductor current feedback is used to create the internal current-loop and this current is compared with the reference current which generate the current error which passed through the PI based current controller and the

resultant signal is compared with the triangular carrier wave to produce the PWM gate pulses for the SEPIC converter switch.

Furthermore, the LLC resonant converter forms the secondary stage. The dc-link voltage is fed to the LLC resonant converter and its output voltage is controlled using PI-voltage controller and resultant frequency signal is processed by the Pulse Frequency Modulation (PFM) which generate the switching pulses for the HB-LLC resonant converter. The schematic of control technique for the proposed EV battery charger is depicted in Fig.4.8.

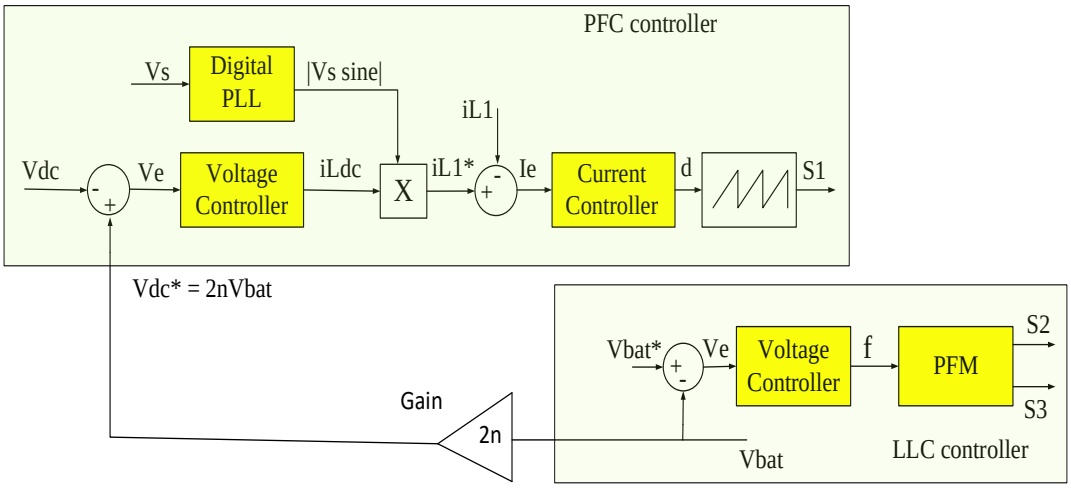

Fig.4.8. Control technique for the proposed EV battery charger.

4.5 Simulation Results

The verification of proposed converter is done on MATLAB/Simulink software. In this section simulation are performed for wide range of battery voltages, various input voltages for different loads.

4.5.1 Verification of Wide Battery voltage range and DC-Link Voltage

The dc-link voltage follows the battery voltage so that $V^*_{dc} = 2nV_{bat}$. The theoretical study of variation of DC-link voltage with respect to the battery voltage is depicted in Fig.4.9. The Vdc* = 252.48V for 48V battery voltage is the minimum voltage and Vdc* = 420.8 V for 80V battery voltage for the maximum battery voltage.

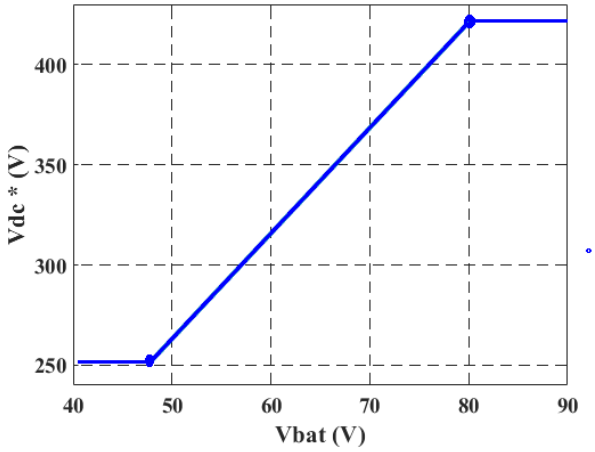

Fig.4.9. DC-link voltage variation with respect to the battery voltages.

The theoretical study is verified by simulation exercise and results are shown in Fig.4.10. The simulation is performed for battery voltage 48V to 80V. The DC-link voltage followed the battery voltage at V_{bat} = 48V the V_{dc} =250V is observed while at V_{bat}= 80V the DC-link voltage V_{dc} = 419V is observed.

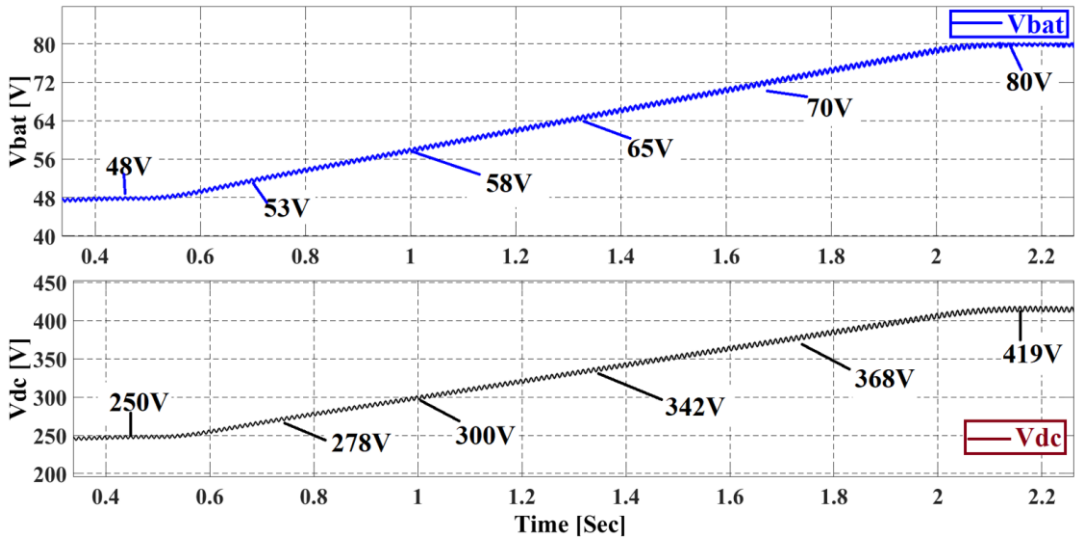

Fig.4.10 DC-link voltage variation w.r.t to battery voltage

4.5.2 Verification of the EV Battery charger under different Supply Voltages

The simulation is performed under various input supply voltage ranges from ($85V_{rms}$-$220V_{rms}$) for the battery voltage V_{bat} = 57V and load P_o = 1kW. The source current shows excellent performance for entire range of source voltage with THD less than 3% with unity power factor. The battery voltage is not affected by the variation of input voltage can be observed from the fig.4.11.

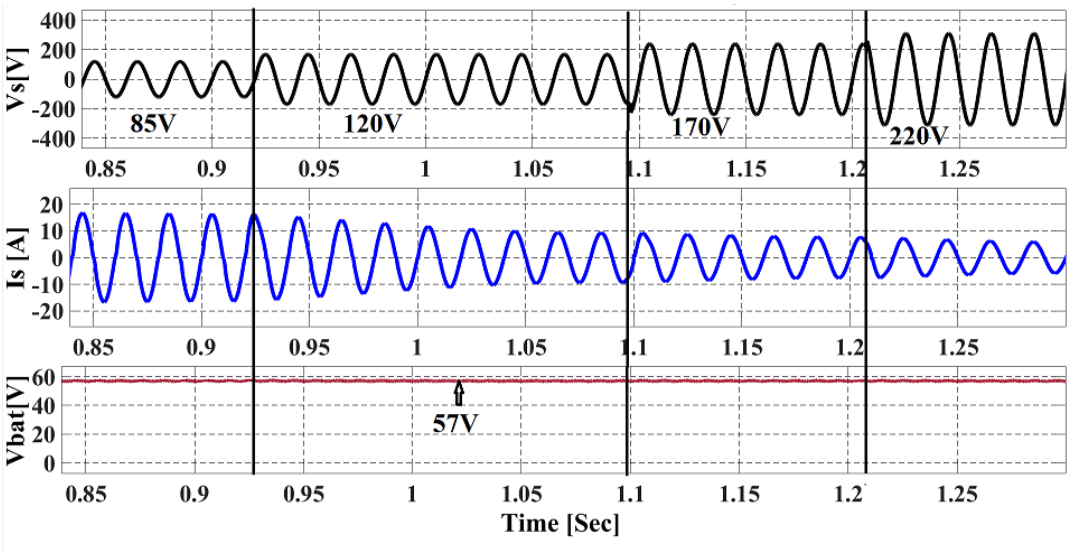

Fig. 4.11. Simulation results of source current, battery voltage under various input voltages.

4.5.3 Verification of the EV battery charger under various loads

The simulation is performed for different loads from high load to light load ranges from 1kW to 100W. The battery voltage kept constant at 57V and load is varied by varying the current of the battery. The maximum current 17.54A is achieved at 1kW and minimum current 1.57A is observed at light load of 100W. At high load slightly more ripple is observed in battery voltage and current in comparison to the light loads. The performance is shown in Fig.4.12.

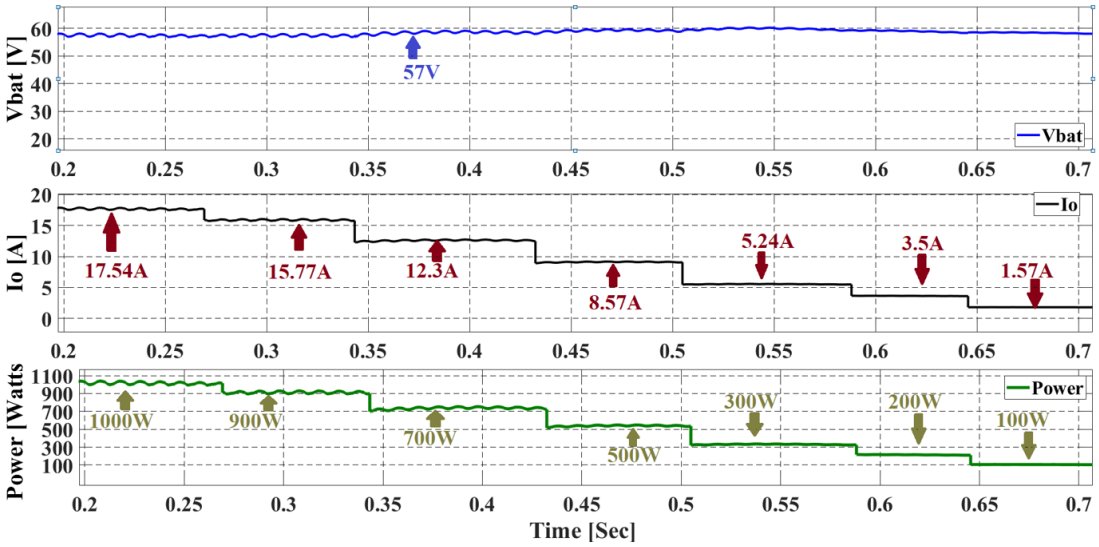

Fig.4.12 Performance of the EV battery charger under various loads.

4.5.4 Performance of EV battery charger at nominal supply and nominal battery voltage

Fig.4.13 demonstrate the operation of the converter at power P_o = 700W and input voltage V_s =220V. It shows that the input current follows the source voltage with unity power factor. The dc-link voltage reaches to 300V for battery voltage 57V. The primary inductor and secondary current are in continuous conduction mode. The waveform of intermediate capacitor is depicted in Fig.4.13 with peak amplitude of 370V. The Fast Fourier Transform (FFT) analysis is shown in Fig.4.14 with TDD 1.61%.

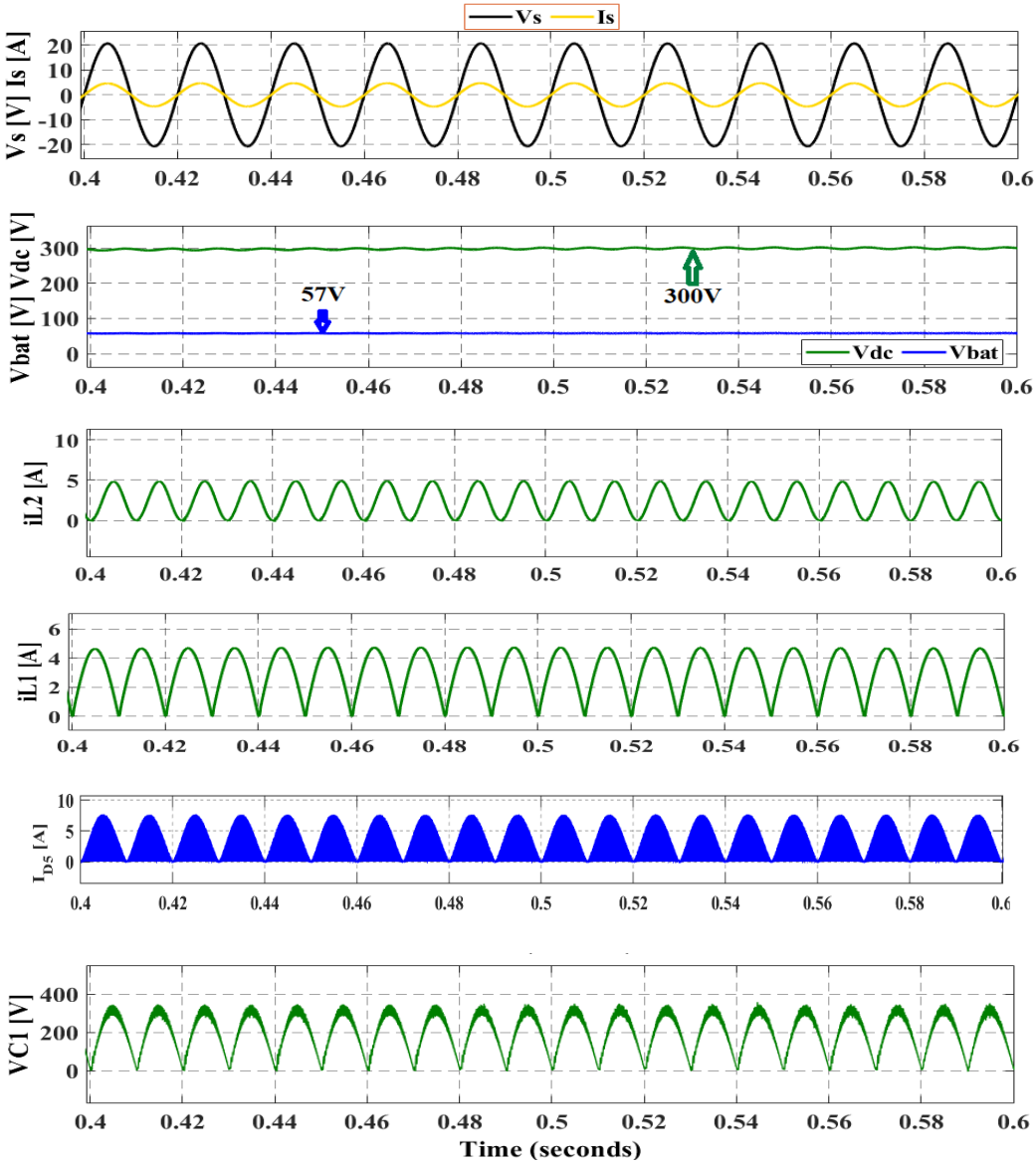

Fig. 4.13. The key waveforms of I_s, V_{dc}, V_{bat}, iL_1, iL_2, I_{D5}, VC1 for P_o = 700W and V_s =220V.

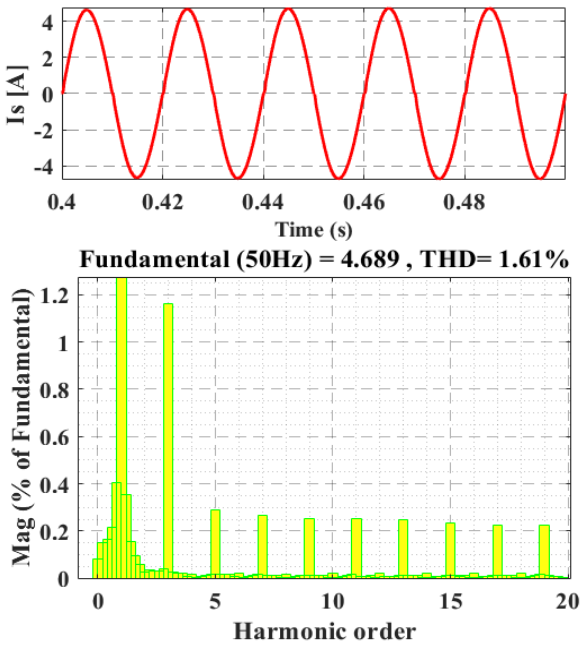

Fig.4.14 Fast Fourier transform analysis of source current for at P_o =700W and V_{bat} = 57V.

The performance of LLC resonant converter is depicted in Fig.4.15. The current waveforms of resonant and magnetizing inductors shows that the LLC resonant converter is operating near the resonance frequency. The peak value across the capacitor is 400V. The voltage and current of MOSFET switch show the zero-voltage switching is achieved.

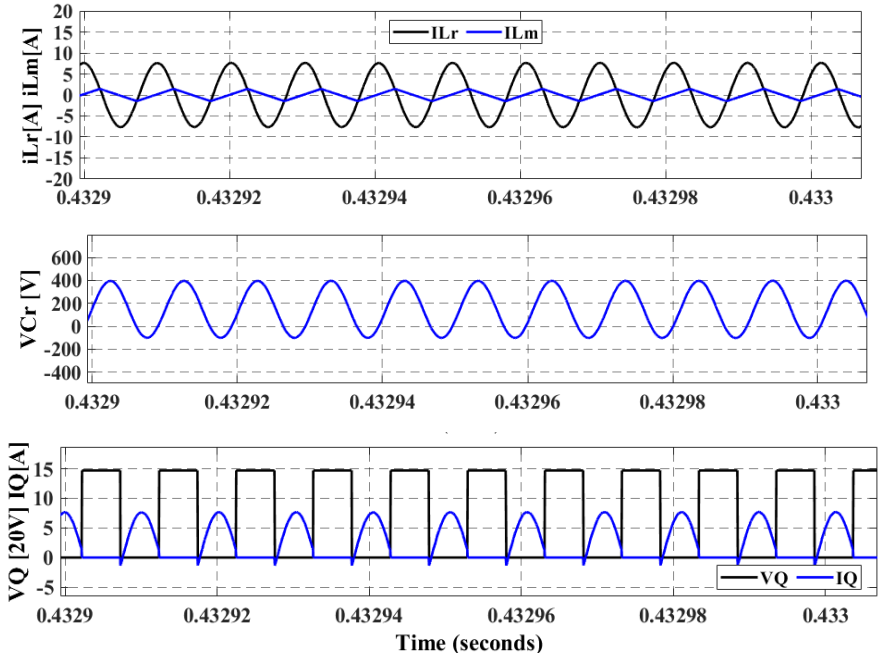

Fig.4.15. The key waveforms of i_{Lr}, i_{Lm}, V_{Cr}, and voltage and current across MOSFET switch for P_o = 700W at V_s = 220V.

4.5.5 Overall performance of the EV battery charger

At various load the proposed technique has better effieciencies in comparision of conventional tenchinque in which DC-link kept constant and wide frequency variation for different loads. The overall efficiency comparison plot is depicted in Fig.4.16. for different loads and overall performance under varous loads, supply voltages and battery voltages are concluded in Table 4.2.

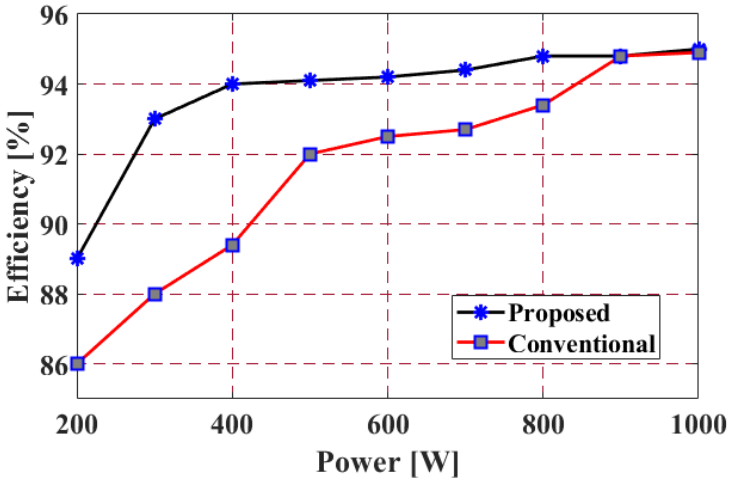

Fig.4.16 Overall efficiency of the battery charger under various load.

Table 4.2 Overall performance of the charger

V_s (V_{rms})	I_s (A_{rm})	V_{dc} (V)	Po (W)	V_{bat}(V)	Io (A)	TDD (%)
220	9.34	419	1970	80	24.63	2.547
220	7.20	368	1508	70	21.53	2.231
220	6.23	342	1300	65	19.89	1.873
220	5.29	315	1107	60	18.45	1.432
220	4.78	300	1000	57	17.54	1.453
170	6.23	300	1000	57	17.54	2.456
120	8.75	300	1000	57	17.54	2.843
85	12.38	300	1000	57	17.54	3.895
220	4.32	300	900	57	15.77	1.553
220	4.10	278	864	53	16.30	1.544
220	3.36	300	700	57	12.30	1.612
220	2.42	300	500	57	8.57	2.021
220	1.45	300	300	57	5.24	2.135
220	1.02	300	200	57	3.50	2.522
220	0.52	300	100	57	1.57	2.656

4.6 Outcomes of Proposed Work

A power factor correction based on SEPIC converter followed by HB-LLC resonant converter has been designed. The LLC resonant converter operated near the resonance frequency for the entire battery voltage range (48-80V). The theoretical design is verified with simulation for various input voltages ($85V_{rms}$-$220V_{rms}$) as well as various battery voltage (48V-80V) at different loads with TDD less than 3.895% for V_s = 85V. However, the overall peak efficiency is achieved 95% at 1kW and 89% at light load which is far better than the conventional method.

CHAPTER 5

BIDIRECTIONAL HALF-BRIDGE LLC RESONANT CONVERTER

5.1 Introduction

A bidirectional half-bridge LLC resonant converter topology for EV battery charging is designed. Fig. 5.1 depicts the schematic of proposed bidirectional converter.

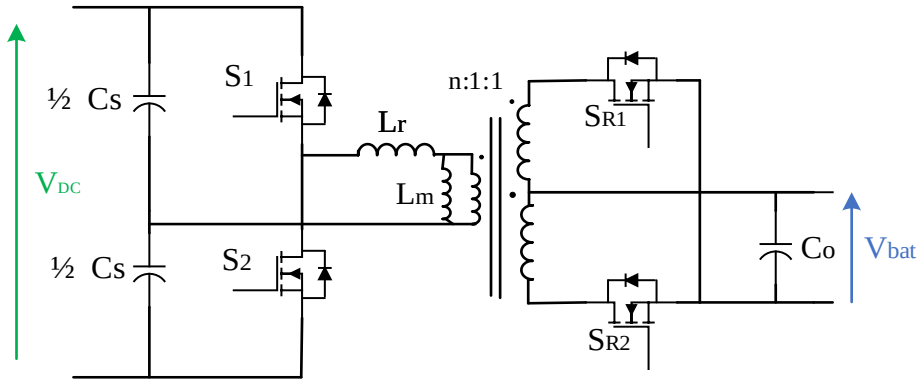

Fig. 5.1 Schematic of bidirectional LLC resonant converter

5.2 Bidirectional LLC half bridge resonant converter analysis

Forward and backward operation are examined in the converter analysis. This architecture has LC series resonance frequency (f_r) and series-parallel resonance frequency (f_{pr}) characteristics for both modes, as defined by equations (5.1) and (5.2), respectively.

$$f_r = \frac{1}{2\pi\sqrt{C_r L_r}} \tag{5.1}$$

$$f_{pr} = \frac{1}{2\pi\sqrt{C_r(L_r + L_m)}} \tag{5.2}$$

Where L_r is the series inductance, L_m is the parallel inductance and C_r is the series capacitance.

During battery charging the converter operate in forward mode in which power flows from ac supply to the battery (G2V) while in battery discharging mode converter operate in backward mode and power flow to the load connected at grid side (V2G).

A fixed duty cycle of 0.5 and variable frequency will be used for the operation of the converter and the first harmonic approximation (FHA) is used for the converter investigation.

5.2.1 Forward mode analysis

In forward mode, the converter is analysed as a conventional unidirectional LLC resonant [66,67,68]. The converter is evaluated as a traditional unidirectional LLC resonant in forward mode [66 67, 68]. The MOSFETs pair (S_1, S_2) and the resonant capacitors on the high-voltage side apply a square wave voltage $V_{HB}(t)$, which can be written as,

$$V_{HB} = \frac{2V_{DC}}{\pi}\sin(\omega_s t) \tag{5.1}$$

Where $\omega_s = 2\pi f_s$ is the switching angular frequency. The AC equivalent circuit for the forward mode of the converter are depicted in Fig.5.2.

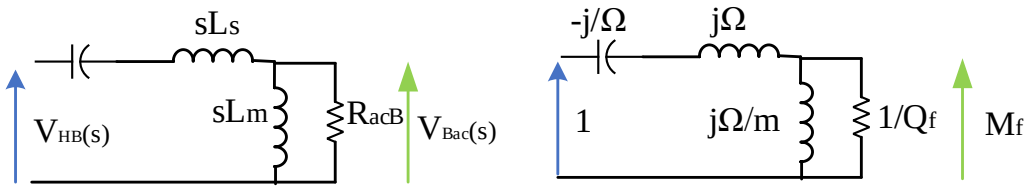

Fig. 5.2 Series-parallel LLC filter in forward mode

The parameters of the converter are defined as,

$$m = \frac{L_r}{L_m} \tag{5.2}$$

$$R_{acB} = \frac{8n^2 {V_{bat}}^2}{\pi^2 P} \tag{5.3}$$

$$n = \frac{V_{DC}}{2V_{bat}} \tag{5.4}$$

$$Z_0 = \sqrt{\frac{L_r}{C_r}} \tag{5.5}$$

$$Q_f = \frac{Z_0}{R_{acB}} \tag{5.6}$$

$$\Omega = \frac{\omega_s}{\omega_r} \tag{5.7}$$

Where m is the ratio of series and parallel inductances, R_{acB} is the equivalent AC resistance of the battery pack reflected to the primary side of transformer, n is the turns ratio. Z_0 is the characteristic impedance of the resonant tank, Q_f is the quality factor in the forward mode and Ω is the normalized frequency.

So, the transfer function of the circuit depicted in fig 5.2 is given as,

$$|M_f| = \frac{\Omega^2}{\sqrt{[\Omega(m+1)-m]^2 + \Omega^2 Q_f^2 (1-\Omega^2)^2}} \tag{5.8}$$

For m = 0.167 gain curve is depicted in fig.5.3 for different values of Q.

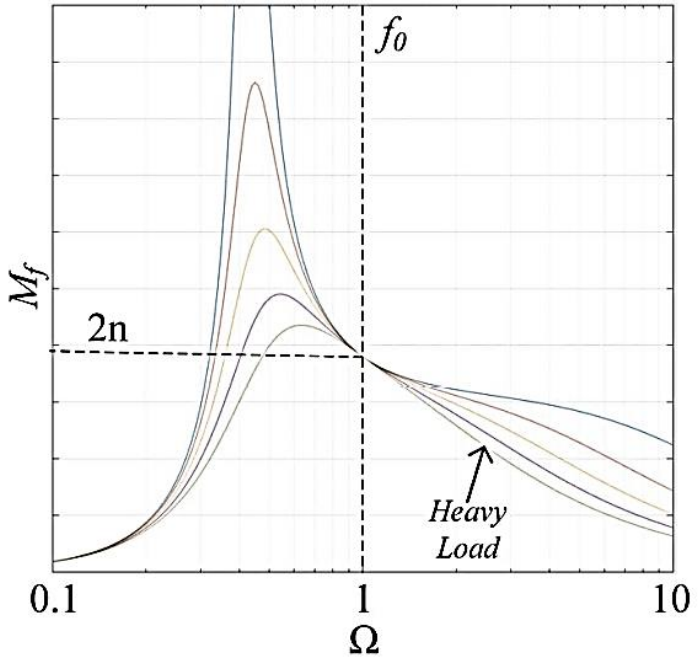

Fig. 5.3 Forward gain as a function of normalized switching frequency

5.2.2 Backward mode analysis

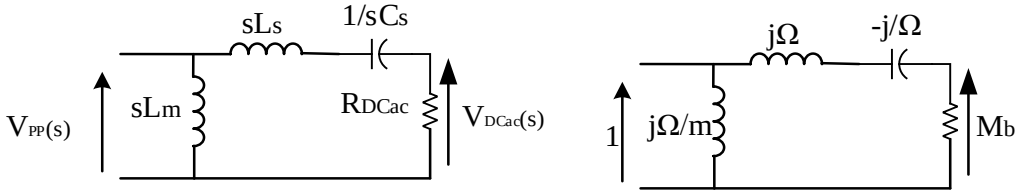

Fig. 5.4 Series-parallel resonant LLC filter in backward mode

Fig. 5.4 illustrate the AC equivalent circuit for the converter's backward mode. In a push-pull converter, the input voltage $V_{PP}(t)$ has a square wave form with characteristics from the terminals input voltage of the transformer. $V_{PP}(t)$ can be

defined by equation in a sinusoidal approximation. $V_{PP}(s)$ is the frequency domain representation of $V_{PP}(t)$.

$$V_{PP} = \frac{4nV_{bat}}{\pi}\sin(\omega_s t) \tag{5.9}$$

The equivalent load for the AC circuit R_{DCac} is shown by equation (5.10).

$$R_{DCac} = \frac{2R_{DC}}{\pi^2} \tag{5.10}$$

where R_{DC} denotes DC load resistance, which varies throughout operation. As a result, in backward operating mode, the quality factor Q_b has been changed to the following equation (5.11) for a characteristic impedance of the resonant filter Z_0 of the same value as in forward operation mode.

$$Q_b = \frac{Z_0}{R_{DCac}} \tag{5.11}$$

The transfer function in backward mode is M_b is given as,

$$|M_b| = \frac{2n\Omega}{\sqrt{Q_b(\Omega^2-1)^2+\Omega^2}} \tag{5.12}$$

For m = 0.167, gain curve is represented in fig.5.5 for different values of Q_b. The ZCS operation on the switched MOSFET occurs for $\Omega < 1$ and ZVS operation occurs for $\Omega > 1$. [69]

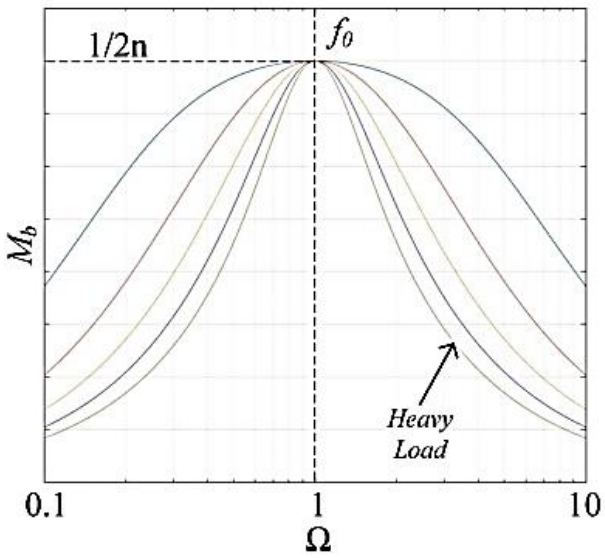

Fig. 5.5 Operating characteristics of Half-Bridge LLC resonant converter in backward mode

5.3 Design Procedure

The design parameters are described in Table 5.1.

Table 5.1 Design Parameters

Parameter	Symbol	Value
DC Bus voltage	V_{DC}	380V
Battery Voltage range	V_{bat}	24V
Maximum Power	P_{max}	292Watts
Turns ratio of transformer	n	10
Series resonance frequency	f_r	20kHz
Series capacitance	C_s	2 x 43 nF
Series Inductance	L_r	800μF
Magnetizing Inductance	L_m	1.2 mH
Inductance ratio	m	0.667
Characteristics Impedance	Z_o	96.45
Quality factor in forward mode	Q_{fmax}	0.6
Quality factor in backward mode	Q_{bmax}	0.96

5.3.1 Forward mode design

Fig. 5.6 shows the battery voltage curves with a dc-link voltage of 380 V (nominal gain), where each curve corresponds to the level of charge of the battery bank. The voltage levels of the battery bank change depending on the state of charge (SOC), indicating that the converter will have a frequency range of about 0.9f_r for these voltage levels. Soft-switching (ZVS turn-on of high-voltage side switches and ZCS turn-off of low-voltage side switches) is used in this region by the LLC resonant converter [66].

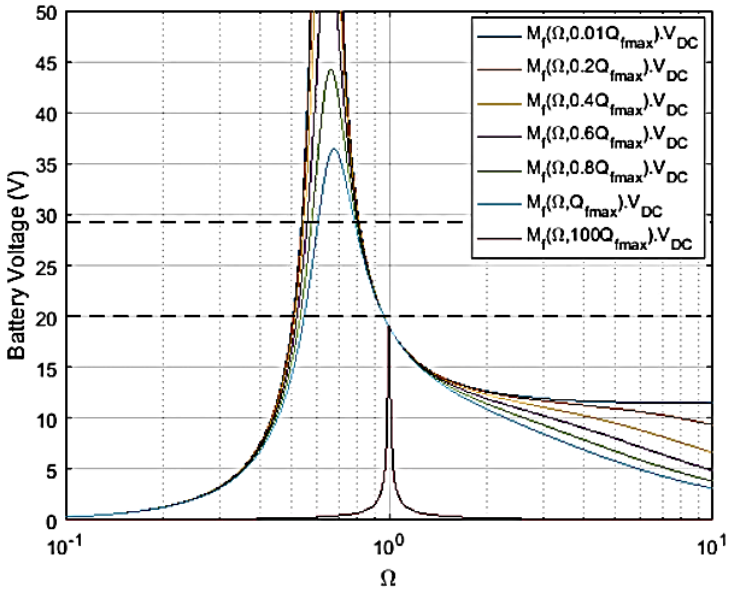

Fig. 5.6 Battery voltage w.r.t to normalized frequency

The battery charging current in maintain using proportional-integral controller. The controller schematic is shown in fig. 5.7

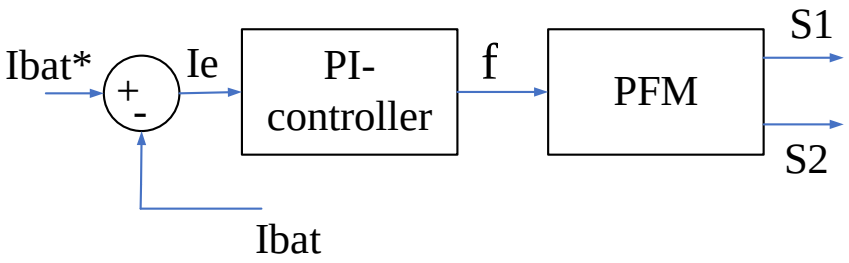

Fig. 5.7 Battery current control schematic

5.3.2 Backward mode design

The voltage oscillates between the fluctuation and the cut-off value as the battery is drained, therefore the converter switching frequency preserves a constant voltage even if the nano-grid load varies. The converter's performance in backward operation mode for minimum and maximum battery voltage is shown in Fig.5.8 and 5.9, respectively. The maximum operating frequency is 20kHz for the worst-case scenario (20 % of nominal load). The control diagram is shown in fig. 5.10.

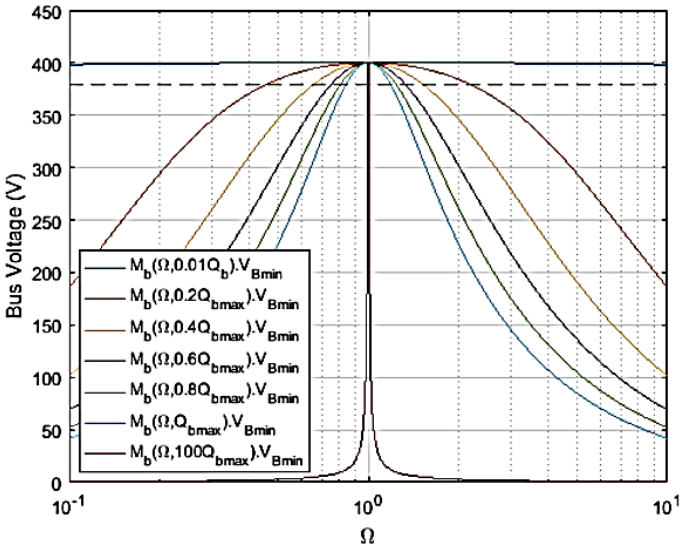

Fig. 5.8 Operating characteristic for LLC half-bridge resonant converter, in backward operation mode for minimum battery voltage.

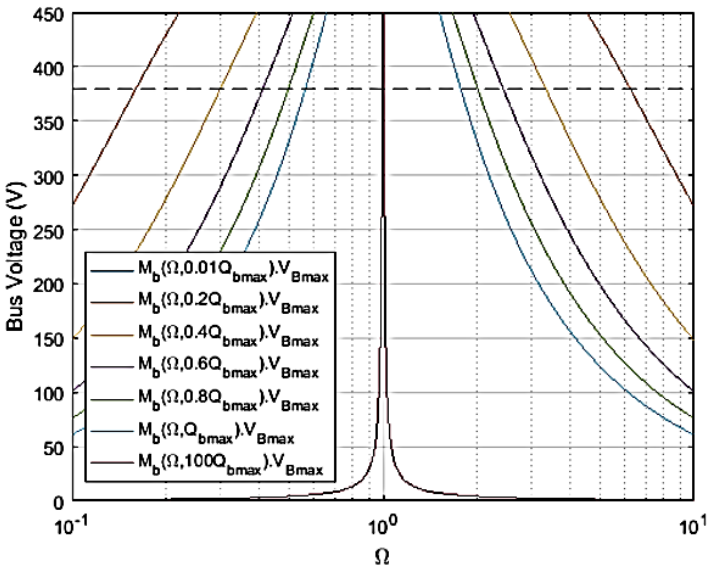

Fig. 5.9 Operating characteristic for LLC half-bridge resonant converter, in backward operation mode for maximum battery voltage.

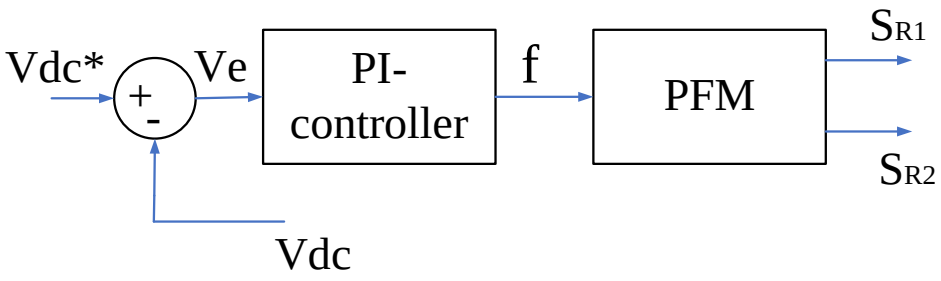

Fig. 5.10 Block diagram of controller in backward mode

5.4 Results

5.4.1 Forward mode

Fig. 5.11 depicts the SOC level which start from 70%, different level of battery charging current for nominal battery voltage of 24V.

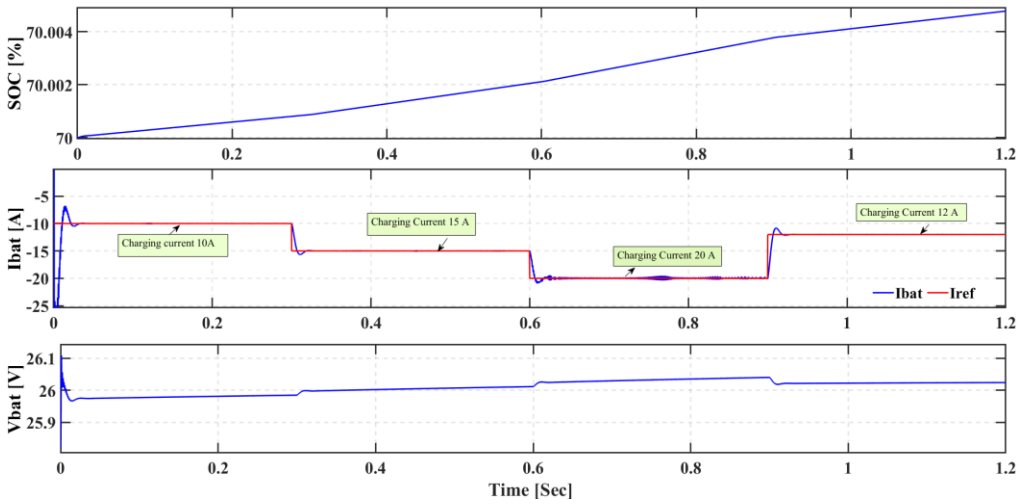

Fig. 5.11 Simulation results of SOC, battery charging current and battery voltage.

Fig. 5.12 shows the ZVS at the switch S_1 and ZCS at switch S_{R1}. Fig. 5.13 depicts the resonant current and magnetizing current waveforms.

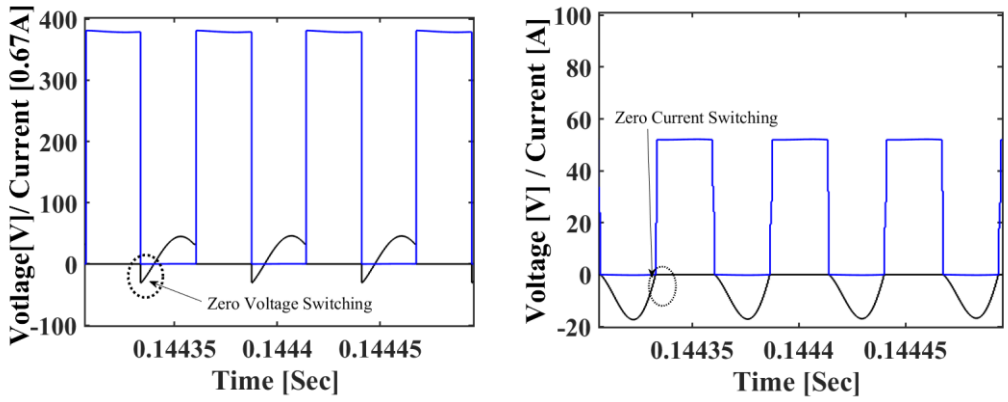

Fig. 5.12 Zero voltage switching and Zero current switching in forward mode

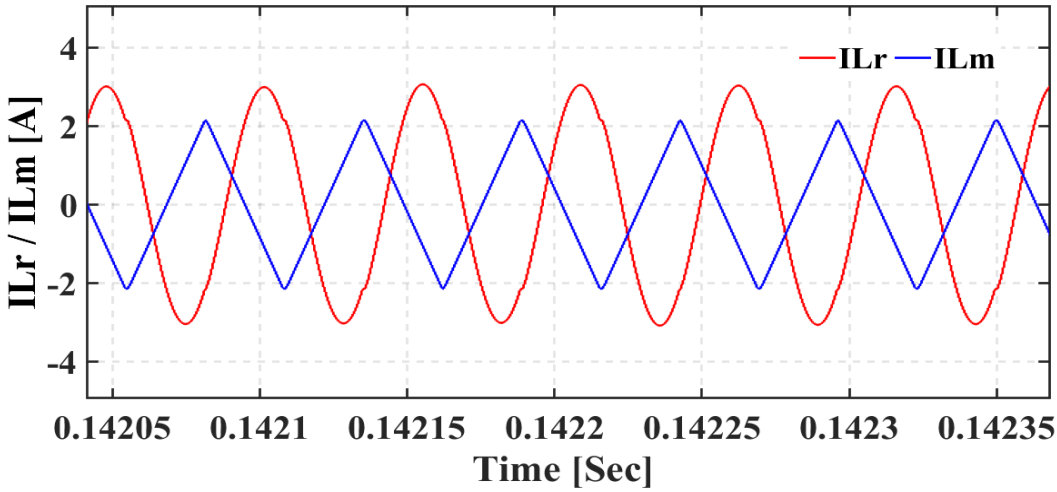

Fig. 5.13 Resonant and Magnetizing current waveform in forward mode

5.4.2 Backward mode

Fig. 5.14 depicts the dc-link voltage which is controlled using the PI-controller at 380V and battery voltage is varying with respect to the frequency, on increasing the switching frequency the current supply from the battery is decreased and on decreasing the switching frequency current supply from the battery is increased which can be observed from the fig. 5.14. Fig. 5.15 shows the ZVS at the switch S_{R1} and ZCS at switch S_1. Fig. 5.16 depicts the resonant current and magnetizing current waveforms.

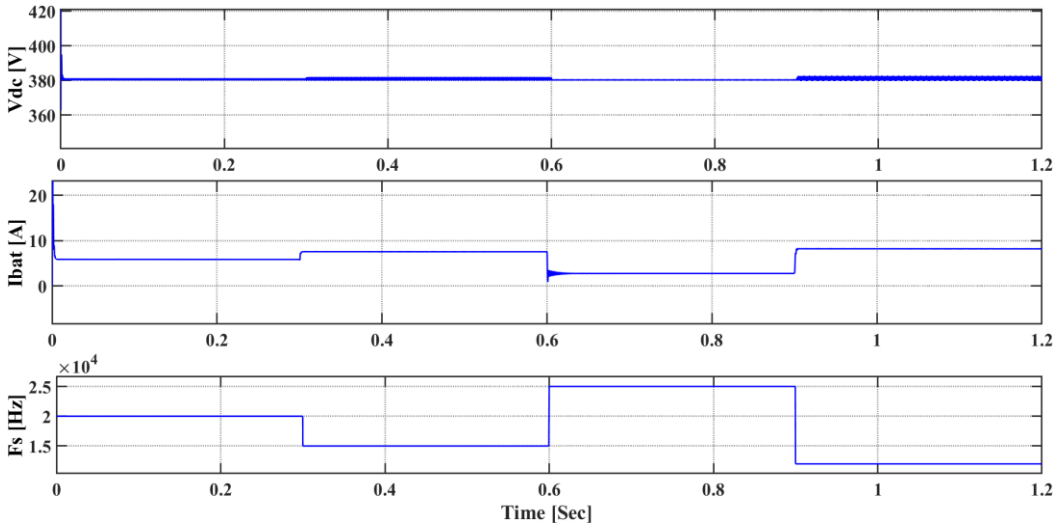

Fig. 5.14 Simulation results of dc-link voltage, Battery current and switching frequency.

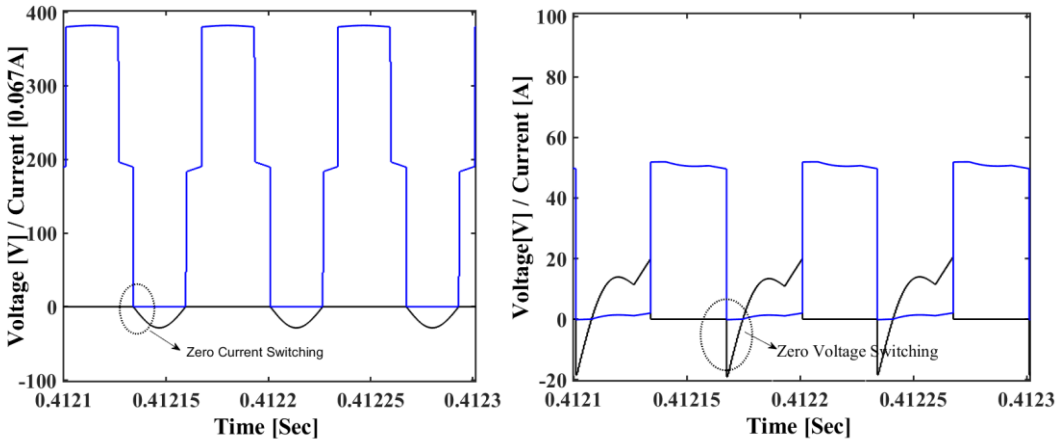

Fig.5.15 Zero current switching and Zero voltage switching in backward mode

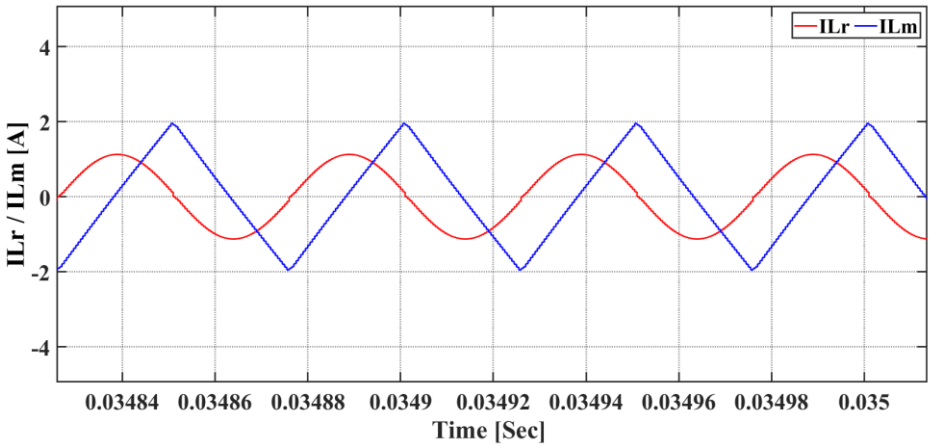

Fig. 5.16 Resonant current and magnetizing current waveforms in backward mode

5.5 Outcome of Proposed Work

There are several advantages observed in bidirectional resonant topology such as soft switching for all the operating range in forward and backward mode of operation. It has capability of transferring power in both the direction.

CHAPTER 6

SENSITIVE ANALYSIS

The novel work of the thesis is summarised as follows:

- a Half-Bridge LLC resonant converter is simulated for the three modes of operation, at resonance frequency, above resonance frequency, below resonance frequency illustrated in chapter 2. The performance under various frequency is obtained in Table. 6.1 and depicted in Fig.6.1.

Table. 6.1 Performance under various frequency

Performances	**$f_s < f_r$**	**$f_s = f_r$**	**$f_s > f_r$**
Turn on loss of MOSFET switch	ZVS	ZVS	ZVS
Turn off loss of MOSFET switch	Low	Low	High
Circulting current on primary side	High	Low	Medium
Secondary diodes	ZCS	ZCS	No
Conduction losses	High	Low	Medium
Switching losses	Low	Low	High
Harmonics	Low	Low	High
Overall Performance	Medium	Best	Medium

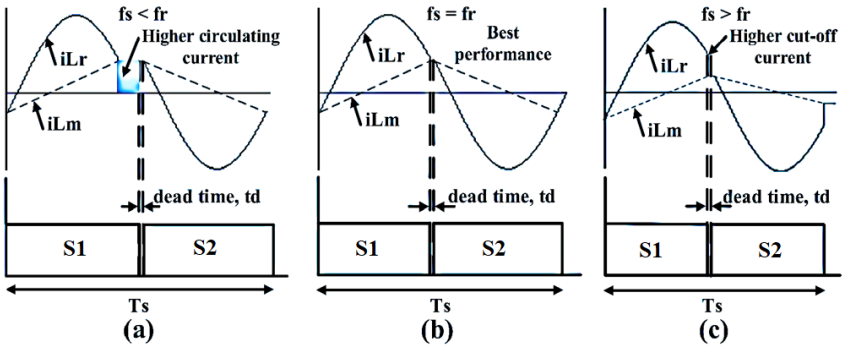

Fig. 6.1. Waveforms of resonant current (i_{Lr}) and magnetizing current waveforms (i_{Lm}) for different operating point (a) $f_s < f_r$ (b) $f_s = f_r$ (c) $f_s > f_r$

It has been also verified for closed loop operation. For different input voltages ranges from 340V- 420V, the output voltage remains constant at 58V as it is well regulated by PI-controller. The efficiency is measured under various load ranges from 400W- 750W and is found very marginal. The peak efficiency is observed as 96.3%.

- The boost converter fed Half-Bridge LLC resonant converter is simulated and performance is analysed under various supply voltages and loads. The battery voltage is regulated at 48V for different input supplies and various loads. The

power factor is measured under various input and it has been observed that the maximum THD is 3.18%. The overall performance is obtained in Table. 6.2.

Table. 6. 2 Overall performance of Boost converter fed LLC

V_s (V)	I_s (A)	PF	THD (%)	P_o (W)
150	4.129	0.99962	2.75	576
160	3.877	0.99966	2.61	576
170	3.643	0.99969	2.48	576
180	3.441	0.99969	2.49	576
190	3.260	0.99971	2.39	576
200	3.097	0.99966	2.60	576
210	2.949	0.99968	2.52	576
220	2.815	0.99965	2.63	576
230	2.693	0.99964	2.70	576
240	2.581	0.99958	2.89	576
250	2.477	0.99953	3.07	576
260	2.382	0.99949	3.18	576

- The SEPIC converter fed Half-Bridge LLC resonant converter is simulated and illustrated in chapter 4. The SEPIC converter has ability to perform buck and boost performance helps supress the large inrush current at supply. The uniqueness of the proposed battery charger are as follows:
    - The unique control technique is adopted so that dc-link voltage of the converter follows the battery voltage and operates near the resonant frequency for optimal operation shown in Fig.6.2.
    - It has the ability to perform wide input voltage ranges ($85V_{rms}$ - $220V_{rms}$) at unity power factor.
    - It also has the ability to charge the battery for a wide range of voltages (48V – 80 V) at high efficiency.
    - It gives excellent performance from light load to full load.

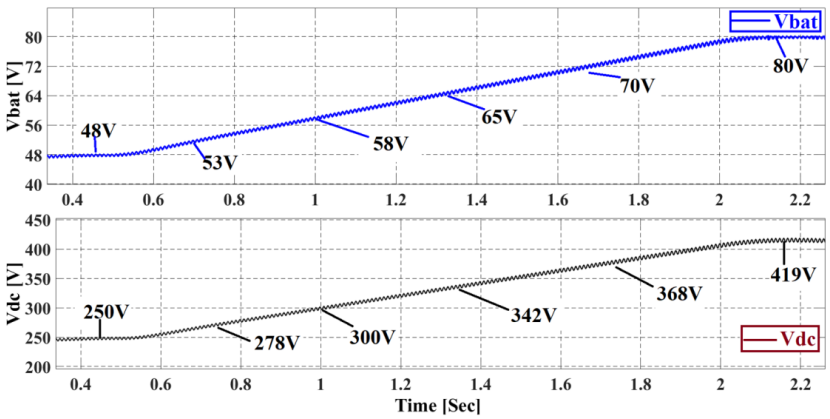

Fig. 6.2 Voltage profile of dc-link and EV battery

The large inrush current issue occurred in boost fed HB-LLC resonant converter is resolved with SEPIC converter due to presence of intermediate capacitor in SEPIC converter. The waveforms of supply current and voltages are depicted in fig.6.3. and fig.6.4.

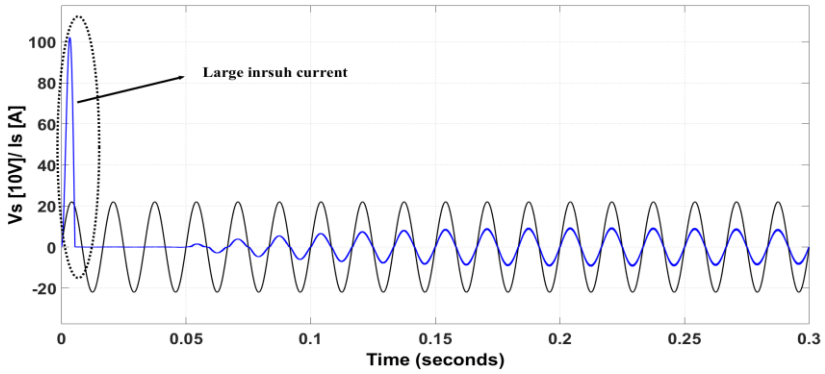

Fig. 6.3. The key waveforms of V_s and I_s of boost converter fed LLC resonant converter

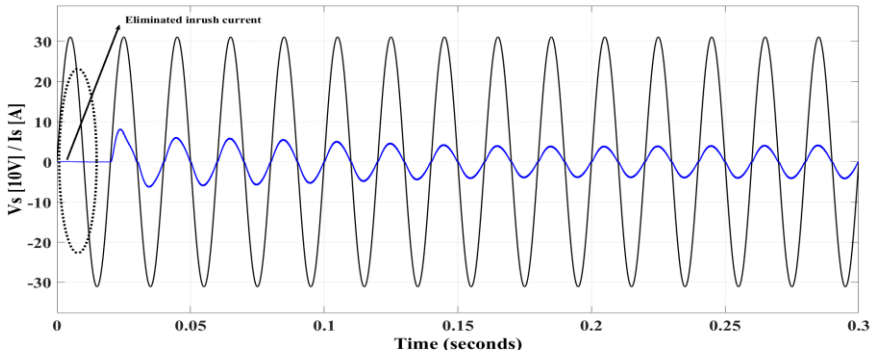

Fig. 6.4. The key waveforms of V_s and I_s of SEPIC converter fed LLC resonant converter

The performance of the SEPIC converter fed Half-Bridge LLC resonant converter is summarized in Table.6.3.

Table.6.3 Overall performance of proposed converter

V_s (V_{rms})	I_s (A_{rm})	V_{dc} (V)	Po (W)	V_{bat}(V)	Io (A)	TDD (%)
220	9.34	419	1970	80	24.63	2.547
220	7.20	368	1508	70	21.53	2.231
220	6.23	342	1300	65	19.89	1.873
220	5.29	315	1107	60	18.45	1.432
220	4.78	300	1000	57	17.54	1.453
170	6.23	300	1000	57	17.54	2.456
120	8.75	300	1000	57	17.54	2.843
85	12.38	300	1000	57	17.54	3.895
220	4.32	300	900	57	15.77	1.553
220	4.10	278	864	53	16.30	1.544
220	3.36	300	700	57	12.30	1.612
220	2.42	300	500	57	8.57	2.021
220	1.45	300	300	57	5.24	2.135

220	1.02	300	200	57	3.50	2.522
220	0.52	300	100	57	1.57	2.656

- A bidirectional half-bridge LLC resonant converter is simulated which is illustrated in chapter 5. There are two mode of operation forward mode and backward mode. In forward mode, the battery is charging and power flows from dc-link to the battery and in backward mode, the battery is supplying the power to the load connected at input side through the dc-link. The charging current is controlled using PI-controller during the battery charging and voltage is maintained across the load during the backward mode of operation. The ZVS and ZCS is achieved in both the mode shown in Fig. 6.5. and Fig.6.6.

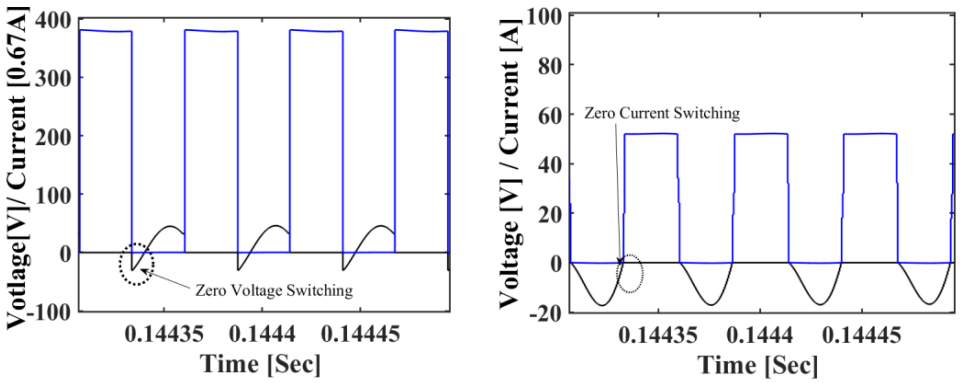

Fig.6.5. ZVS and ZCS in forward mode

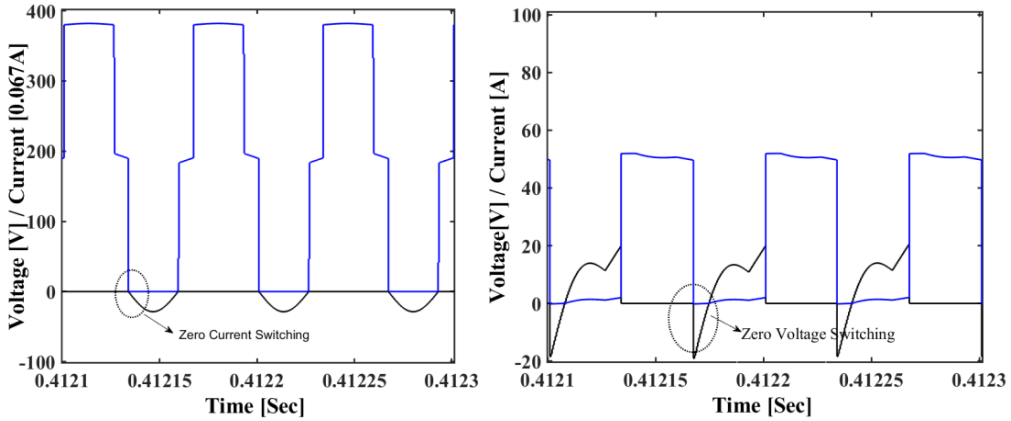

Fig.6.6. ZCS and ZVS in backward mode

CHAPTER 7
CONCLUSION AND FUTURE WORK

7.1 Work summary

AC-DC on-board electric vehicle battery charger is designed and simulated on MATLAB Simulink environment. Initially, a Half-Bridge LLC resonant converter is designed and simulated under various frequencies, at resonance frequency, above resonance frequency and below resonance frequency. It has obtained that the LLC resonant converter gives it better performance near the resonance frequency. Futhermore, a Half-Bridge LLC resonant converter is integrated with boost converter power factor correction at it has been obtained that it improves the power quality of AC supply current with maximum THD 3.18% illustrated in chapter 3. Apart from this another observation is noted that it suffers from large inrush input current at the supply side for 8.36 msec. To eliminate the large inrush current, the SEPIC fed half-bridge LLC resonant converter is designed. The presence of intermediate capacitor in SEPIC supresses the inrush current which is illustrated in chapter 7. It has been also observed that the SEPIC converter performs well for universal supply voltage ranges from 85 V_{rms} – 220V_{rms} and various power rating ranges from 2kW to 100 W. The DC-link voltage of the SEPIC fed LLC resonant converter is following the battery voltage to operate near resonance frequency for improved performance illustrated in chapter 5. Furthermore, bidirectional LLC resonant converter has been designed to operate in forward mode for battery charging for grid to battery and in backward mode for supply power to load connected at grid side. It has been noted that it achieves ZVS and ZCS in both the mode at different level of charging and discharging of the battery.

7.2 Future Work

The hardware implementation of Half-Bridge LLC resonant converter can be done in future with the power factor correction circuit to commercialized the prototype model.

REFRENCES

[1] M. Kesler, M. Kisacikoglu, and L. Tolbert, "Vehicle-to-Grid Reactive Power Operation Using Plug-in Electric Vehicle Bidirectional Off-Board Charger," IEEE Transactions on Industrial Electronics, vol. PP, pp. 1-1, 2014.

[2] J. C. Mukherjee and A. Gupta, "A Review of Charge Scheduling of Electric Vehicles in Smart Grid," IEEE Systems Journal, vol. 9, pp. 1541-1553, 2015

[3] C. C. Chan, "An overview of electric vehicle technology," Proceedings of the IEEE, vol. 81, pp. 1202-1213, 1993.

[4] Z. Xiaohu, S. Lukic, S. Bhattacharya, and A. Huang, "Design and control of grid-connected converter in bi-directional battery charger for Plug-in hybrid electric vehicle application," in Vehicle Power and Propulsion Conference, 2009. VPPC '09. IEEE, 2009, pp. 1716-1721.

[5] Y. Ota, H. Taniguchi, T. Nakajima, K. M. Liyanage, J. Baba, and A. Yokoyama, "Autonomous Distributed V2G (Vehicle-to-Grid) Satisfying Scheduled Charging," IEEE Transactions on Smart Grid, vol. 3, pp. 559-564, 2012.

[6] U. K. Madawala and D. J. Thrimawithana, "A Bidirectional Inductive Power Interface for Electric Vehicles in V2G Systems," IEEE Transactions on Industrial Electronics, vol. 58, pp. 4789-4796, 2011.

[7] H. Liu, Z. Hu, Y. Song, and J. Lin, "Decentralized Vehicle-to-Grid Control for Primary Frequency Regulation Considering Charging Demands," IEEE Transactions on Power Systems, vol. 28, pp. 3480-3489, 2013.

[8] M. Yilmaz and P. T. Krein, "Review of the Impact of Vehicle-to-Grid Technologies on Distribution Systems and Utility Interfaces," IEEE Transactions on Power Electronics, vol. 28, pp. 5673-5689, 2013.

[9] M. Yilmaz and P. T. Krein, "Review of Battery Charger Topologies, Charging Power Levels, and Infrastructure for Plug-In Electric and Hybrid Vehicles," IEEE Transactions on Power Electronics, vol. 28, pp. 2151-2169, 2013.

[10] A. Westgeest and L. Brett, "Improving safety and performance testing for EV batteries," in 2013 World Electric Vehicle Symposium and Exhibition (EVS27), 2013, pp. 1-4.

[11] P. A. Cassani and S. S. Williamson, "Significance of Battery Cell Equalization and Monitoring for Practical Commercialization of Plug-In Hybrid Electric

Vehicles," in 2009 Twenty-Fourth Annual IEEE Applied Power Electronics Conference and Exposition, 2009, pp. 465-471.

[12] A. Khaligh and Z. Li, "Battery, Ultracapacitor, Fuel Cell, and Hybrid Energy Storage Systems for Electric, Hybrid Electric, Fuel Cell, and Plug-In Hybrid Electric Vehicles: State of the Art," IEEE Transactions on Vehicular Technology, vol. 59, pp. 2806-2814, 2010.

[13] P. Ramadass, B. Haran, R. White, and B. N. Popov, "Performance study of commercial LiCoO2 and spinel-based Li-ion cells," Journal of Power Sources, vol. 111, pp. 210-220, 9/23/ 2002.

[14] K. Nihal, "Rechargeable batteries and battery management systems design," in IECON 2010 - 36th Annual Conference on IEEE Industrial Electronics Society, 2010, pp. 1-2.

[15] J. T. Salihi, P. D. Agarwal, and G. J. Spix, "Induction Motor Control Scheme for Battery-Powered Electric Car (GM-Electrovair I)," IEEE Transactions on Industry and General Applications, vol. IGA-3, pp. 463-469, 1967.

[16] S. Jurkovic, K. M. Rahman, and P. J. Savagian, "Design, optimization and development of electric machine for traction application in GM battery electric vehicle," in 2015 IEEE International Electric Machines & Drives Conference (IEMDC), 2015, pp. 1814-1819.

[17] P. Leijen and N. Kularatna, "Developing a monitoring system for Toyota Prius battery-packs for longer term performance issues," in 2013 IEEE International Symposium on Industrial Electronics, 2013, pp. 1-6.

[18] K. J. Kelly, M. Mihalic, and M. Zolot, "Battery usage and thermal performance of the Toyota Prius and Honda Insight during chassis dynamometer testing," in Seventeenth Annual Battery Conference on Applications and Advances. Proceedings of Conference (Cat. No.02TH8576), 2002, pp. 247-252.

[19] W. Renhart, C. Magele, and B. Schweighofer, "FEM-Based Thermal Analysis of NiMH Batteries for Hybrid Vehicles," IEEE Transactions on Magnetics, vol. 44, pp. 802-805, 2008.

[20] A. Hoke, A. Brissette, K. Smith, A. Pratt, and D. Maksimovic, "Accounting for Lithium-Ion Battery Degradation in Electric Vehicle Charging Optimization," IEEE Journal of Emerging and Selected Topics in Power Electronics, vol. 2, pp. 691-700, 2014

[21] J. R. M. D. Reyes, R. V. Parsons, and R. Hoemsen, "Winter Happens: The Effect of Ambient Temperature on the Travel Range of Electric Vehicles," IEEE Transactions on Vehicular Technology, vol. 65, pp. 4016-4022, 2016.

[22] O. Tremblay, L. A. Dessaint, and A. I. Dekkiche, "A Generic Battery Model for the Dynamic Simulation of Hybrid Electric Vehicles," in 2007 IEEE Vehicle Power and Propulsion Conference, 2007, pp. 284-289.

[23] H. He, R. Xiong, X. Zhang, F. Sun, and J. Fan, "State-of-Charge Estimation of the Lithium-Ion Battery Using an Adaptive Extended Kalman Filter Based on an Improved Thevenin Model," IEEE Transactions on Vehicular Technology, vol. 60, pp. 1461-1469, 2011.

[24] H. S. Park, C. E. Kim, C. H. Kim, G. W. Moon, and J. H. Lee, "A Modularized Charge Equalizer for an HEV Lithium-Ion Battery String," IEEE Transactions on Industrial Electronics, vol. 56, pp. 1464-1476, 2009.

[25] A. Affanni, A. Bellini, G. Franceschini, P. Guglielmi, and C. Tassoni, "Battery choice and management for new-generation electric vehicles," IEEE Transactions on Industrial Electronics, vol. 52, pp. 1343-1349, 2005.

[26] S. Dey, B. Ayalew, and P. Pisu, "Combined estimation of State-of-Charge and State-of-Health of Li-ion battery cells using SMO on electrochemical model," in 2014 13th International Workshop on Variable Structure Systems (VSS), 2014, pp. 1-6.

[27] R. Milligan, T. Muneer, and I. Smith, "A comparative range approach using the Real-world Drive Cycles and the Battery Electric Vehicle," in 2015 IEEE International Transportation Electrification Conference (ITEC), 2015, pp. 1-5.

[28] Y. Attia, A. Abdelrahman, M. Hamouda, and M. Youssef, "SiC devices performance overview in EV DC/DC converter: A case study in a Nissan Leaf," in 2016 IEEE Transportation Electrification Conference and Expo, Asia-Pacific (ITEC Asia-Pacific), 2016, pp. 214-219.

[29] W. Liangrong, L. Jianing, X. Guoqing, X. Kun, and S. Zhibin, "A novel battery charger for plugin hybrid electric vehicles," in Information and Automation (ICIA), 2012 International Conference on, 2012, pp. 168-173.

[30] S. R. Osman, N. A. Rahim, and S. Jeyraj, "Single current sensor with multiple constant current charging method in solar battery charger," in 3rd IET International Conference on Clean Energy and Technology (CEAT) 2014, 2014, pp. 1-5.

[31] Y. D. Lee and S. Y. Park, "Rapid charging strategy in the constant voltage mode for a high-power Li-Ion battery," in 2013 IEEE Energy Conversion Congress and Exposition, 2013, pp. 4725-473

[32] S. Li, C. Zhang, and S. Xie, "Research on Fast Charge Method for Lead-Acid Electric Vehicle Batteries," in Intelligent Systems and Applications, 2009. ISA 2009. International Workshop on, 2009, pp. 1-5.

[33] S. G. Abeyratne, P. S. N. Perera, H. S. Jayakody, S. M. K. B. Samarakoon, and R. R. S. De Bulathge, "Soft Switching fast charger for batteries used in Renewable Energy applications and electric vehicles," in Industrial and Information Systems (ICIIS), 2012 7th IEEE International Conference on, 2012, pp. 1-6.

[34] M. Chen and G. A. Rincon-Mora, "Accurate, Compact, and Power-Efficient Li-Ion Battery Charger Circuit," IEEE Transactions on Circuits and Systems II: Express Briefs, vol. 53, pp. 1180- 1184, 2006.

[35] L. Yi-Hwa, T. Jen-Hao, and L. Yu-Chung, "Search for an optimal rapid charging pattern for lithium-ion batteries using ant colony system algorithm," IEEE Transactions on Industrial Electronics, vol. 52, pp. 1328-1336, 2005.

[36] S. A. Singh and S. S. Williamson, "Comprehensive review of PV/EV/grid integration power electronic converter topologies for DC charging applications," in 2014 IEEE Transportation Electrification Conference and Expo (ITEC), 2014, pp. 1-5.

[37] S. S. Williamson, A. K. Rathore, and F. Musavi, "Industrial Electronics for Electric Transportation: Current State-of-the-Art and Future Challenges," IEEE Transactions on Industrial Electronics, vol. 62, pp. 3021-3032, 2015.

[38] A. Dubey and S. Santoso, "Electric Vehicle Charging on Residential Distribution Systems: Impacts and Mitigations," IEEE Access, vol. 3, pp. 1871-1893, 2015.

[39] S. Chalia, A. K. Seth and M. Singh, "Electric Vehicle Charging Standards in India and Safety Consideration," 2021 IEEE 8th Uttar Pradesh Section International Conference on Electrical, Electronics and Computer Engineering (UPCON), 2021, pp. 1-6.

[40] T. Kang, C. Kim, Y. Suh, H. Park, B. Kang, and D. Kim, "A design and control of bi-directional non-isolated DC-DC converter for rapid electric vehicle

charging system," in 2012 IEEE International Conference on Information and Automation, 2012, pp. 14-21.

[41] International Organization for Standardization (ISO). ISO 6469-3:2011 Electrically propelled road vehicles -- Safety specifications -- Part 3: Protection of persons against electric shock Available: http://www.iso.org/iso/catalogue_detail?csnumber=45479

[42] UL. (2016, 10 December). UL 2231-1 Standard for Safety for Personnel Protection Systems for Electric Vehicle (EV) Supply Circuits: General Requirements. Available: https://standardscatalog.ul.com/standards/en/standard_2231-1_2

[43] S. Y. Kim, H. S. Song, and K. Nam, "Idling Port Isolation Control of Three-Port Bidirectional Converter for EVs," IEEE Transactions on Power Electronics, vol. 27, pp. 2495-2506, 2012.

[44] S. Pala and S. P. Singh, "Design, modeling and implementation of Bi-directional buck and boost converter," in 2012 IEEE 5th India International Conference on Power Electronics (IICPE), 2012, pp. 1-6.

[45] A. Nasiri, Z. Nie, S. B. Bekiarov, and A. Emadi, "An On-Line UPS System With Power Factor Correction and Electric Isolation Using BIFRED Converter," IEEE Transactions on Industrial Electronics, vol. 55, pp. 722-730, 2008.

[46] G. Oggier, G. O. García, and A. R. Oliva, "Modulation Strategy to Operate the Dual Active Bridge DC-DC Converter Under Soft Switching in the Whole Operating Range," IEEE Transactions on Power Electronics, vol. 26, pp. 1228-1236, 2011.

[47] M. N. Kheraluwala, R. W. Gascoigne, D. M. Divan, and E. D. Baumann, "Performance characterization of a high-power dual active bridge," IEEE Transactions on Industry Applications, vol. 28, pp. 1294-1301, 1992.

[48] G. G. Oggier, G. O. GarcÍa, and A. R. Oliva, "Switching Control Strategy to Minimize Dual Active Bridge Converter Losses," IEEE Transactions on Power Electronics, vol. 24, pp. 1826-1838, 2009.

[49] M. H. Ryu, H. S. Kim, J. W. Baek, H. G. Kim, and J. H. Jung, "Effective Test Bed of 380-V DC Distribution System Using Isolated Power Converters," IEEE Transactions on Industrial Electronics, vol. 62, pp. 4525-4536, 2015.

[50] T. Jiang, X. Chen, J. Zhang, and Y. Wang, "Bidirectional LLC resonant converter for energy storage applications," in 2013 Twenty-Eighth Annual IEEE Applied Power Electronics Conference and Exposition (APEC), 2013, pp. 1145-1151.

[51] X. Xie, Z. Zhao, C. Zhao, J. M. Zhang, and Z. Qian, "Analysis and Optimization of LLC Resonant Converter With a Novel Over-Current Protection Circuit," IEEE Transactions on Power Electronics, vol. 22, pp. 435-443, 2007.

[52] R. Liu and C. Q. Lee, "The LLC-type series resonant converter-variable switching frequency control," in Proceedings of the 32nd Midwest Symposium on Circuits and Systems, 1989, pp. 509- 512 vol.1.

[53] K. Siri and C. Q. Lee, "Constant switching frequency LLC-type series resonant converter," in Circuits and Systems, 1989., Proceedings of the 32nd Midwest Symposium on, 1989, pp. 513-516 vol.1.

[54] C. J and W. A. F., "Analytic solutions for LLCC parallel resonant converter simplify use of two and three-element converters," IEEE Transactions on Power Electronics, vol. 13, pp. 235-243, 1998.

[55] G. Y, L. Z, and Q. Z, "Three level LLC series resonant DC/DC converter," in 2004 Nineteenth Annual IEEE Applied Power Electronics Conference and Exposition (APEC), 2004, pp. 1647- 1652 Vol.3.

[56] B. Yang, F. C. Lee, A. J. Zhang, and H. Guisong, "LLC resonant converter for front end DC/DC conversion," in Applied Power Electronics Conference and Exposition, 2002. APEC 2002. Seventeenth Annual IEEE, 2002, pp. 1108-1112 vol.2.

[57] C. Gould, C. M. Bingham, D. A. Stone, and M. P. Foster, "CLL resonant converters with output short-circuit protection," Electric Power Applications, IEE Proceedings -, vol. 152, pp. 1296-1306, 2005.

[58] C. Gould, D. A. Stone, M. P. Foster, and C. Bingham, "State-variable modelling of CLL resonant converters," in Second International Conference on Power Electronics, Machines and Drives (PEMD 2004). 2004, pp. 214-219 Vol.1.

[59] C. H. Chang, C. Hung-Liang, C. En-Chih, C. Chun-An, and C. Hung-Yi, "Modeling and design of the LLC resonant converter used in solar array simulator," in 2012 7th IEEE Conference on Industrial Electronics and Applications (ICIEA), 2012, pp. 653-658.

[60] G. Pledl, M. Tauer, and D. Buecherl, "Theory of operation, design procedure and simulation of a bidirectional LLC resonant converter for vehicular applications," in 2010 IEEE Vehicle Power and Propulsion Conference, 2010, pp. 1-5.

[61] F. Krismer, J. Biela, and J. W. Kolar, "A comparative evaluation of isolated bi-directional DC/DC converters with wide input and output voltage range," in Fourtieth IAS Annual Meeting. Conference Record of the 2005 Industry Applications Conference, 2005., 2005, pp. 599-606 Vol. 1.

[62] Hong Huang, “Designing an LLC Resonant Half-Bridge Power Converter,” Texas Instruments (TI) Power Supply Design Seminar, SEM1900, 2010, TI Literature No. SLUP263.

[63] Sam Abdel-Rahman, "Resonant LLC Converter: Operation and Design" Infineon Technologies North America (IFNA) Corp. Application Note AN 2012-09 V1.0 September 2012.

[64] A. Anand and B. Singh, “Design and implementation of PFC Cuk converter fed SRM drive,” IET Power Electronics, vol. 10, no. 12, pp. 1539-1549, 2017.

[65] A. J. Sabzali, E. H. Ismail, M. A. Al-Saffar and A. A. Fardoun, “New bridgeless DCM Sepic and Cuk PFC rectifiers with low conduction and switching losses,” IEEE Transactions on Industry Applications, vol. 47, no. 2, pp. 873-881, 2011.

[66] Jee-hoon Jung and Joong-gi Kwon. Theoretical analysis and optimal design of llc resonant converter. In Power Electronics and Applications, 2007 European Conference on, pages 1–10. IEEE, 2007.

[67] Bo Yang, Fred C Lee, AJ Zhang, and Guisong Huang. Llc resonant converter for front end dc/dc conversion. In Applied Power Electronics Conference and Exposition, 2002. APEC 2002. Seventeenth Annual IEEE, volume 2, pages 1108–1112. IEEE, 2002.

[68] Bo Yang, Rengang Chen, and Fred C Lee. Integrated magnetic for llc resonant converter. In Applied Power Electronics Conference and Exposition, 2002. APEC 2002. Seventeenth Annual IEEE, volume 1, pages 346– 351. IEEE, 2002.

[69] Sihun Yang, Seiya Abe, Toshiyuki Zaitsu, Junichi Yamamoto, Masahito Shoyama, and Tamotsu Ninomiya. Consideration of operating characteristics for bidirectional llc resonant converter. International Journal of Renewable Energy Research (IJRER), 2(4):790–796, 2012.

LIST OF PUBLICATION

1. **Design and Simulation of a Half-Bridge LLC Resonant Converter for Battery Charger in EV.**

   R. Maurya and R. Saha, "Design and Simulation of a Half-Bridge LLC Resonant Converter for Battery Charger in EV," 2022 IEEE Delhi Section Conference (DELCON), 2022, pp. 1-9, doi: 10.1109/DELCON54057.2022.9753654.